

HIGH-FIELD MAGNETS WITH AND WITHOUT FERROMAGNETIC RETURN YOKES*

H. Brechna
Stanford Linear Accelerator Center
Stanford University, Stanford, California 94305

J. Perot**
Commissariat a l'Energie Atomique, Saclay, France

SUMMARY

The main purpose of this paper is to illustrate the effect of ferromagnetic materials on field enhancement and field distribution in a useful magnet aperture. Also treated are the effects of perturbations due to manufacturing constraints.

A selected number of magnet types was chosen, such as axially-symmetric magnets, and higher order coils. The field distribution is calculated in the presence or absence of iron return yokes. The field values are obtained by using computer codes for variable permeability problems based on vector potential calculations. Computational results are compared to simplified first-order calculation methods utilizing uniform permeability distribution or infinite permeability in iron.

To show the extent of perturbations due to coil manufacturing upon field or gradient homogeneity in beam transport magnets, a calculating method based on complex variables is used. Field or gradient distribution in the coil aperture, due to ideal current density distribution, is compared to flux densities or field gradients when the ideal coil configuration has been modified to a more practical shape. Current filaments (multi-poles) are used to correct for field inhomogeneities.

Computer calculations have their limitations due to convergence problems, size limitation, digitalization, and boundary effects. Specifically, if field homogeneity in the order of 10^{-5} over a certain experimental area is required, computational errors overshadow actual results due to the presence of iron with variable iron permeability or partial saturation. Based on a practical 8th-order coil, a computational method is illustrated, which overcomes this deficiency.

I. INTRODUCTION

Ferromagnetic flux return paths have been used in magnets since 1911. New types of laboratory magnets were introduced by Du Bois. Weiss, Dreyfuss, Fabry, and Bitter incorporated improvements in iron shaping, utilizing uniform and optimum magnetization in iron poles and yokes.¹ Bitter used iron return yokes in magnets with 10-T central fields. Most of these magnets had a high-field volume of only a few cm³.

*Work supported by the U. S. Atomic Energy Commission.

**Guest at Stanford Linear Accelerator Center in 1969.

Large magnets with a working space of several m^3 and magnetic fields in the order of ≤ 2 T have been built by several laboratories. In magnets with higher fields, due to iron saturation, the coil must generate the major part ($\geq 90\%$) of the magnetic field. In these magnets (≥ 3 T), field-shaping must also be performed mainly by correcting coils. Thus iron yokes were abandoned, e.g., in superconducting or cryogenic magnets, for a short time for magnets generating fields of 5 T or higher. As shielding is mandatory for most experiments to protect instruments and equipment, iron as a flux return path became attractive again. Iron enhances, at the same coil excitation, the central field, yields more balanced force conditions, and may be used as part of the coil support structure.

Methods to calculate the effect of iron on the magnitude and distribution of the field within the magnet aperture had to be extended to obtain accurate data. From early assumptions of uniform iron magnetization or infinite iron permeability, a more sophisticated computational method was developed to solve "quasi-Poisson" equations with variable iron permeability by means of difference equations. The computer codes now available are SYBYL,² TRIM,³ POISSON,⁴ MARE,⁵ and NUTCRACKER,⁶ to name only a few. Parallel to this development, complex variables were used extensively by Beth⁷ and Halbach,⁸ to calculate the magnetic fields of coils and iron-bound magnets.

It is well understood that by utilizing iron as a flux return path, either the field in the useful magnet aperture is enhanced or the coil MMF can be accordingly reduced, if the same field amplitude is being sought. It is a general assumption, however, that due to non-uniform magnetization of iron, the field homogeneity of a magnet is no longer guaranteed and thus, specifically in high-precision 6th- and 8th-order coils, the iron return yoke may cause more harm than good. Utilization of the iron flux path serves several important functions:

1. Properly designed, it shields the fringing field around the magnet and makes it possible to locate counters, photomultipliers, and other test devices close to the magnet.
2. It enhances the field in the center. As to how much (we will give some simplified calculating methods), this depends on the iron geometry, the amount of iron being placed around the coil, and the proximity of iron to the coil.
3. It tends to reduce the forces between coils, due to reduction of the magnetic field energy (split coil arrangement). For cryogenic and superconducting magnets, the iron return yoke may be used to support dewars and vacuum vessels.
4. The reduction in MMF is not trivial and in saturated iron, this reduction may exceed 10% of the total MMF. In non-superconducting magnets, the power reduction may be considerable. In the case of superconducting magnets, the coils may be smaller and superconducting material may be saved.
5. Magnet time constant is increased. When a superconducting coil quenches, the iron return path acts as a secondary transformer winding and prevents coil damage.

In high-field magnets, one important property of the iron is lost: the field-shaping property. As the relative permeability approaches unity, the iron surface is no longer equipotential. Field-shaping is now entirely due to the magnet coil configuration, and correcting coils, if required. However, methods of field-shaping by means of superconducting screens and sheets become more attractive and are being attempted for large-aperture spark and wire chamber magnets.

Although we are basically studying high-field magnets, where the field at the conductor is in the order of 5 T or more, we will show that the role of iron is not merely for shielding and thus of minor importance, but that it affects substantially the overall

field configuration within the useful aperture of the magnet. If iron is placed symmetrically around the coil, the field homogeneity obtained by the coil alone is not only reduced but may be improved.

In this paper, we study various types of magnets, such as beam transport magnets with and without return yokes, iron-bound solenoids, dipole-type magnets for use in wire or spark chambers, and high-homogeneity magnets. Methods of computer calculations are not given here. There is a vast amount of literature available for study. We give simplified calculation methods based on actual measurements and comparative computation.

In high-field magnets, where field generation is dominated by the coils, any perturbation effect is important. We study only a few: misplaced coil configurations, and shifted or askew coils. We also present simple methods of field correction.

Coil end effects are more pronounced in high-field magnets and may adversely affect the beam dynamics. The end effects cannot be corrected with iron shaping. We summarize the result of the three-dimensional coil end effect calculation and present a method of field-correcting, using superconducting screens or superconducting shields.

II. MAGNETIC FIELD EQUATIONS FOR TWO-DIMENSIONAL COILS AND IRON CORES

Coils. The magnetic field in a two-dimensional space due to a conductor of arbitrary shape (Fig. 1) and overall current density λJ is given by⁹:

$$H^* = \frac{\lambda J}{4\pi} \oint_c \frac{Z^* - Z_0^*}{Z - Z_0} dz \quad (1)$$

with:

$$H^* = H_X - jH_Y$$

$$Z = X + jY$$

$$Z^* = X - jY \quad j = (-1)^{1/2}$$

Equation (1) is valid for all points in space, both inside and outside the coil region.

The field gradient is obtained from Eq. (1) by differentiation:

$$G^* = \frac{\partial H^*}{\partial Z_0} = \frac{\partial H_X}{\partial X_0} - j \frac{\partial H_Y}{\partial X_0}$$

which yields:

$$G^* = \frac{\lambda J}{4\pi} \oint_c \frac{Z^*}{(Z - Z_0)^2} dz \quad (2)$$

We approximate the arbitrary coil shape by a polygon, consisting of n straight lines, each having the equation:

$$X = aY + b$$

where a and b are general complex constants of the form:

$$a = \frac{X_{k+1} - X_k}{Y_{k+1} - Y_k}$$

$$b = \frac{X_k \cdot Y_{k+1} - X_{k+1} \cdot Y_k}{Y_{k+1} - Y_k}$$

$$\frac{b}{a} = \frac{Y_k(X_k - X_{k+1})}{X_{k+1} - X_k} = -Y_k$$

and obtain for the field at Z_0 :

$$H^* = \frac{\lambda J}{2\pi} \sum_{k=1}^N \frac{j}{(j+a_k)} (a_k \cdot Y_0 + b_k - X_0) \ln \left(\frac{Z_{k+1} - Z_0}{Z_k - Z_0} \right) \quad (3)$$

$$G^* = \frac{\lambda J}{4\pi} \sum_{k=1}^N \cdot \left(\frac{a_k - j}{a_k + j} \right) \ln \left(\frac{Z_{k+1} - Z_0}{Z_k - Z_0} \right) \quad (4)$$

To obtain field multipole coefficients, we expand the field in a power series over a region excluding all currents:

$$H^*(Z_0) = \sum_{n=1}^{\infty} C_n \cdot Z_0^{n-1} \quad (5)$$

with

$$C_n = \frac{\lambda J}{4\pi} \oint \frac{Z^*}{Z^n} dZ \quad (6)$$

In particular:

$$C_1 = \frac{\lambda J}{2\pi} \sum_{k=1}^N \frac{j}{a_k + j} \cdot b_k \ln \left(\frac{Z_{k+1}}{Z_k} \right)$$

If $a \rightarrow \infty$,

$$C_1 = \frac{\lambda J}{2\pi} \sum_{k=1}^N -j \cdot Y_k \ln \left(\frac{Z_{k+1}}{Z_k} \right)$$

For $n \geq 3$:

$$C_n = \frac{\lambda J}{2\pi} \sum_{k=1}^N j \cdot \frac{1}{(a_k + j)} \left[\frac{a_k - j}{2j} \cdot \frac{Z_{k+1}^{2-n} - Z_k^{2-n}}{2-n} - b_k \cdot \frac{Z_{k+1}^{1-n} - Z_k^{1-n}}{1-n} \right] \quad (7)$$

With the specific case of $a \rightarrow \infty$,

$$C_n = \frac{\lambda J}{2\pi} \sum_{k=1}^N j \left[\frac{1}{2j} \frac{Z_{k+1}^{2-n} - Z_k^{2-n}}{2-n} - Y_k \frac{Z_{k+1}^{1-n} - Z_k^{1-n}}{1-n} \right]$$

Field corrections. The magnetic field due to a current filament is given by

$$H^* = j \cdot \frac{I}{2\pi} \cdot \frac{1}{Z - Z_0} \quad (8)$$

If N wires parallel to each other are placed on the circumference of a circle (Fig. 2), the total field is accordingly:

$$\begin{aligned} H^* &= j \frac{I}{2\pi} \sum_1^N \frac{1}{Z - Z_0} = \sum_1^{\infty} C_n Z_0^{n-1} \\ &= j \frac{I}{2\pi} \sum_1^N \frac{1}{Z \left(1 - \frac{Z_0}{Z}\right)} = j \frac{I}{2\pi} \sum_1^N \frac{1}{Z} \sum_1^{\infty} \frac{Z_0^{n-1}}{Z^{n-1}} \end{aligned} \quad (9)$$

In Eq. (9):
 $n = 1$ corresponds to $N = 2$ (dipole configuration)
 $n = 2$ corresponds to $N = 4$ (quadrupole configuration)

General: $2n = N$ for a multipole,

and

$$C_n = j \frac{I}{2\pi} \sum_{m=1}^{2n} \frac{(-1)^{m-1}}{Z^m} \quad (10)$$

as the complex constant.

To cancel any perturbation indicated by a field coefficient, one places a current filament I at a selected place. The current filament is located such that the vector \vec{C}_n is perpendicular to the radius vector r . The sign of the current is given by the sign of the real part of C_n and the magnitude of the current by

$$I = \text{real} \left(\frac{C_n}{\frac{j}{2\pi} \sum_{m=1}^{2n} \frac{(-1)^{m-1}}{Z^m}} \right) \quad (11)$$

Contribution of iron (simplified assumptions). Field distribution of a multipole air core magnet surrounded by iron is given by Blewett.¹⁰ For coils having finite thickness

(Fig. 3) and the iron permeability being infinite, we express the two field components by:

$$B_x = \frac{2\mu_0}{\pi} \lambda J \cdot \left\{ \frac{1}{2-n} (a_2^{2-n} - a_1^{2-n}) \cdot \frac{\sqrt{3}}{2} + \frac{1}{(n+2)b_1^{2n}} (a_2^{n+2} - a_1^{n+2}) \right\} \cdot r^{n-1} \cdot \sin n\theta \quad (12)$$

$$B_y = \frac{2\mu_0}{\pi} \lambda J \cdot \left\{ \frac{1}{2-n} (a_2^{2-n} - a_1^{2-n}) \cdot \frac{\sqrt{3}}{2} - \frac{1}{(n+2)b_1^{2n}} (a_2^{n+2} - a_1^{n+2}) \right\} \cdot r^{n-1} \cdot \cos n\theta$$

for $r \leq a_1$, and

$$B_x = \frac{2\mu_0}{\pi} \lambda J \cdot \left[\frac{r^{n-1}}{b_1^{2n}} + \frac{\sqrt{3}}{2} \cdot \frac{1}{r^{n+1}} \right] \left(\frac{1}{n+2} \right) (a_2^{n+2} - a_1^{n+2}) \cdot \sin n\theta \quad (13)$$

$$B_y = \frac{2\mu_0}{\pi} \lambda J \cdot \left[\frac{r^{n-1}}{b_1^{2n}} - \frac{\sqrt{3}}{2} \cdot \frac{1}{r^{n+1}} \right] \left(\frac{1}{n+2} \right) (a_2^{n+2} - a_1^{n+2}) \cdot \cos n\theta$$

for $r \geq a_1$.

In Eq. (12) and (13), the coil aperture and the iron shell are assumed to be circular. In all multipoles considered, we assume constant average current density distribution over the coil cross-sectional area, but each coil section may follow the two-thirds rule expanding over a sector of n poles. $n=1$ applies to a dipole, $n=2$ to a quadrupole, etc. To determine the thickness of iron surrounding the coils, field calculations based on variable iron permeability indicate that for all values of $B \geq 1$ T, the flux density distribution in the yoke is according to:

$$B = B_2 \cdot \left(\frac{B_1}{B_2} \right)^{\frac{x-b_2}{b_1-b_2}}$$

with B_1 being the field at the inner radius b_1 and B_2 at the outer radius b_2 . The flux density is reduced considerably over the last outer part of the iron boundary where $B \leq 1$ T, as seen from several field plots for circular iron shields given in Fig. 4.

In polygonally-shaped multipoles, the field distribution over the iron cross section has a slight drop along the X and Y directions. We may assume in this case an average value of B for a first approximation to calculate iron contribution. This is also observed in axially symmetric magnets, which makes computation simpler. For all values of $r \geq a_2$, which is the iron region, the two field components are written in the form:

$$B_x = \frac{2\mu_0}{\pi} \lambda J \cdot \left(\frac{r^{n-1}}{b_1^{2n}} + \frac{1}{r^{n+1}} \right) \left(\frac{1}{n+2} \right) \cdot (a_2^{n+2} - a_1^{n+2}) \cdot \sin n\theta$$

$$B_y = \frac{2\mu_0}{\pi} \lambda J \cdot \left(\frac{r^{n-1}}{b_1^{2n}} - \frac{1}{r^{n+1}} \right) \left(\frac{1}{n+2} \right) \cdot (a_2^{n+2} - a_1^{n+2}) \cdot \cos n\theta$$

Similar equations are derived for multipole magnets with straight yoke portions, such as in the case of a polygon. As an example, for a square quadrupole, we may write:

$$B_x = \frac{2\mu_0}{\pi} \lambda J \cdot \left[\tan^{-1} \frac{a_2^2 - a_1^2}{4a_1 a_2} + \frac{1}{4b_1^4} (a_2^4 - a_1^4) \right] r \cdot \sin n \theta \quad (14)$$

The above equations permit determination of the iron thickness. However, these calculations do not give more accurate results than about 8%. The assumption of an average relative permeability and uniform magnetization is not justified in most high-field iron-bound magnets.

Contribution of iron (exact two-dimensional calculations). In order to determine the field in a two-dimensional configuration, the equation

$$\frac{1}{\mu} \nabla^2 \vec{A} + \nabla \mu \times (\nabla \times \vec{A}) + \vec{J} = 0 \quad (15)$$

must be solved. In our particular case, J and A have only z components, and thus we may write:

$$\nabla \cdot \frac{1}{\mu} \nabla A(x,y) + J(x,y) = 0 \quad (16)$$

or explicitly in Cartesian coordinates:

$$\frac{1}{\mu} \left(\frac{\partial^2 A}{\partial x^2} + \frac{\partial^2 A}{\partial y^2} \right) + \frac{1}{\mu_x} \frac{\partial A}{\partial x} + \frac{1}{\mu_y} \frac{\partial A}{\partial y} + J(x,y) = 0 \quad (17)$$

which is known as the "non-linear" Poisson equation. In cylindrical coordinates, Eq. (17) is written:

$$\frac{1}{\mu} \cdot \left(\frac{\partial^2 A}{\partial r^2} + \frac{\partial^2 A}{\partial z^2} \right) + \frac{1}{\mu_r} \frac{\partial A}{\partial r} + \frac{1}{\mu_z} \frac{\partial A}{\partial z} + \frac{1}{r} \left(\frac{1}{\mu_r} A_z + \frac{1}{\mu_z} A_r \right) - \frac{1}{r^2} \left(\frac{1}{\mu} A \right) + J(r,z) = 0 \quad (18)$$

In Eq. (17) and (18), the permeability

$$\frac{1}{\mu} = \frac{1}{\mu} (A_x, A_y) = \frac{1}{\mu} (A_r, A_z)$$

depends only on the magnitude of the field.

It is not the purpose of this paper to derive solutions of Eq. (17) or (18) by means of approximations through finite difference equations. The method of finite differences results through a process of discretization. Numerical approximations to the continuum problem are given at a finite set of points. These points (meshpoints) are separated by a characteristic distance h, and the field components, in terms of potentials U, are expressed by:

$$B_x = \frac{U_E - U_W}{2h} \quad B_y = \frac{U_N - U_S}{2h} \quad (19)$$

with

$$U_E = u_{i+1,j} \quad U_W = u_{i-1,j} \quad U_N = u_{i,j+1} \quad U_S = u_{i,j-1} \quad U_0 = u_{i,j}$$

with u_i the potential at the point $(P_{i,j})$ at which we are performing the calculation. The assumption of h being constant yields a truncation error of $O(h^2)$, which may be adequate for a variety of magnets, but is not useful for high-homogeneity, higher-order coils.

If U_0 represents the average value of the continuous function $u(x,y)$ over a region R , then expanding U_E or U_W , etc., about U_0 at the point of interest in a Taylor series yields:

$$U_E = U_0 + \left(\frac{\partial u}{\partial x}\right)_0 h_E + \left(\frac{\partial^2 u}{\partial x^2}\right)_0 \frac{h_E^2}{2!} + \left(\frac{\partial^3 u}{\partial x^3}\right)_0 \frac{h_E^3}{3!} + \dots \quad (20)$$

where we assumed $h_E = h_W = \dots = h$.

The accuracy of the problem depends, of course, on the mesh size (the choice of h), which is a function of the storage capacity of the modern computer. The various presently available computational methods, their efficiency, accuracy, and speed of convergence, depend on a number of basic, but fundamental, assumptions, such as iteration methods, choice of boundaries (Neumann, Dirichlet), location of external $A = 0$ or $A = \text{constant}$ boundaries to confine the problem, use of single or double precision methods, etc.

The earliest method for solving the variable permeability problem is given by Trutt,¹¹ where he solved difference equations by the method of over-relaxation (SOR).

Erdelyi and Ahamed¹² solve the equation for the vector potential. In addition to the SOR parameter, they introduced an accelerating method for convergence by computing

$$C_i = \frac{s_i \int J_i dA}{\oint H dl} \quad (21)$$

$$0.96 \leq C \leq 1.04$$

around each conductor.

Perin¹³ developed, in program MARE, a modified scalar potential ϕ^* , satisfying the condition:

$$\nabla \phi^* = H - M \quad (22)$$

The programs use square mesh.

The most active group in solving nonlinear magnetostatic problems is the LRL group, which has developed TRIM and, with modifications, POISSON. Winslow¹⁴ derives difference equations by the use of Gauss's theorem. His equations are of the form:

$$\sum_{n=1}^6 W_n (U_n - U_0) + J = 0 \quad (23)$$

where W_n corresponds to the length of the sides of the triangular meshes used in these programs. The truncation error in this program with regular triangular meshes is in the order

$$-\frac{3}{32} h^4 (\nabla^4 u)_0$$

whereas for a rectangular mesh, the leading term for approximation is of the order

$$-\frac{h^2}{12} (\nabla^4 u)_0$$

Another program (NUTCRACKER), developed at SLAC,⁶ is similar to the programs developed by other groups. The results of the SLAC program are used for calculating some of the high-field magnets described below.

In large two-dimensional or axially-symmetric systems, where the number of meshpoints may exceed 3×10^4 , the basic questions are the time of convergence, the time necessary for one iteration, and the convergence limit for a required accuracy! Several methods of SOR, as well as methods of choosing and calculating the SOR parameter ω , are given in literature. The convergence can be accelerated markedly when ω is varied with the number of iterations. As long as $\omega \leq \omega_F$, the problem is stable, where

$$\omega_F = 2 - \pi (2)^{1/2} \left[\frac{1}{p^2} + \frac{1}{q^2} \right]^{1/2} \quad (24)$$

$$1 \leq \omega \leq 2$$

is the Franckel extrapolation parameter, and p and q are the number of meshpoints in the x and y or r and z directions, respectively.

The general approach to most computer codes is the choice of an arbitrary μ value and an SOR parameter $\omega \leq \omega_F$. The number of iterations can be limited by the selection of a convergence value generally in the order of 10^{-6} . If double precision is used, which results in reducing the number of meshpoints and thus the dimensional accuracy of the problem, the convergence value may reach 10^{-7} . Results obtained using one of the computational methods and compared to measurements are in agreement within 0.1%. The results may not be attractive for high-precision magnets. Some newer computer codes use calculation methods where variable mesh sizes could be used.¹⁵ This method is of special attraction if precise field values in the useful magnet aperture are required. Boundary matching may prove to be a problem. Three-dimensional computation methods are reported by Caeymaex¹⁶ and Halacsy.¹⁷

III. FERROMAGNETIC PROPERTIES OF IRON

In the course of solving magnetostatic problems of iron-bound and iron-core magnets, the permeability of iron must be recalculated numerous times during the iterative process. Any large-sized magnet of 10^4 nodes may require between 250 to 500 iterations. One must calculate the permeability $2.5 \times 10^6 - 5 \times 10^6$ times! The usual method is to find the values of permeability from tabulated experimental data and use extrapolation methods to obtain intermittent data.

Magnetization properties as a function of impurities are reported by Gerold¹⁸ and Brechna.¹⁹ Cold work (cold rolling), grain orientation, and annealing procedures have profound effects upon magnetization properties and thus any computer code should use, as a subroutine, experimental data for the particular iron used for the magnet being considered.

Modern steels used in d. c. magnets have an impurity content ($N_2 + S + P + Al + Mo$) of less than 0.1%, ($Cr + Cu + Mn + Ni + Si$) of less than 0.7%. Carbon, which is the most dangerous impurity, is limited to 0.1%. However, steels recently developed in Japan,²⁰ have a carbon content of less than 0.005%! Pure iron is costly and too soft to be machined and handled for magnet cores. Si has been alloyed to the steel to about 0.1%, which improves mechanical strength without reducing saturation flux density appreciably. A search in literature shows that no data for H greater than 10^5 A/m are available for any steels. As iron is being used for high-field magnets (pulsed or superconducting), the field computation necessitates the extension of the magnetization curve to values of $H > 10^8$ A/m. The experimental law observed for specific magnetization at high fields is given by:

$$m = m_s \left(1 - a/H - b/H^2 \right) + \kappa_0 H \quad (25)$$

with m_s the saturation magnetization and κ_0 the initial susceptibility of iron. The value of M_s from measurements of m_s by Danan *et al.*²¹ is:

$$M_s = 2.1936 \text{ T}$$

The induction B can be determined from M_s as shown in Fig. 5. The magnetization curve is subdivided into four regions:

Region I:	$0 \leq H \text{ (A/m)} \leq 1.6 \times 10^2$	$0 \leq M \text{ (T)} \leq 9.148 \times 10^{-1}$
Region II:	$1.989 \times 10^2 \leq H \text{ (A/m)} \leq 1.592 \times 10^4$	$1.1 \leq M \text{ (T)} \leq 1.910$
Region III:	$2 \times 10^4 \leq H \text{ (A/m)} \leq 1.000 \times 10^8$	$1.95 \leq M \text{ (T)} \leq 2.1936$
Region IV:	$10^8 \leq H \text{ (A/m)} \leq 10^{10}$	$M = 2.1936 \text{ T}$

Each region may now be fitted by second-order splines involving low-order polynomials. The position of joints was optimized by the program developed by Smith²² using an iterative graphic method. The errors due to curve fitting to the experimental data are in the order of 10^{-2} or less, which is adequate if one realizes that different iron specimens vary in their composition to produce uncertainty at least in the same order of magnitude.

IV. AXIALLY SYMMETRIC SYSTEMS

We consider two distinct aspects of iron shielding:

- (a) The economical aspect
 - (b) The field enhancement in the aperture and possible field redistribution due to non-uniform iron magnetization
- (a) To study the impact of an iron return yoke upon the magnet cost, one has several solutions from which to choose: Comparison of small-bore-diameter, high-field magnets to low-field, large-bore magnets, based on effective length comparison. We also may compare magnets of equal size and equal fields, but if non-superconducting magnets are compared to superconducting magnets, it can be shown that above a central field of 3 T, the power consumption in conventional magnets would be exorbitant. Thus we deviate from the goal of studying 5-T or higher field magnets, and compare magnets having a central field of 2.6 T. This also enables us to compare data with magnets already built.

We consider a split-coil arrangement with an inner useful bore diameter of 1.4 m and a central field of 2.6 T. The series of magnets given in Tables I and II are optimized. The magnets compared are a coil with copper conductor, aluminum conductor, liquid-hydrogen-cooled magnet, and a superconducting magnet, with and without iron return yokes. The prices calculated are based on current values. In the tables, $\beta_1 = (2b + g)/a_1$ is half the axial length of the coil, and $\beta_2 = g/a_1$ the axial coil separation.

The two tables (I and II) show that in the field range of ≤ 3 T, room temperature and superconducting magnets are comparable pricewise. The magnets with iron return yokes are less expensive compared to coils without iron return yokes. Cryogenic magnets, thanks to the high resistivity of strained copper and aluminum conductor at liquid hydrogen temperature (which is their optimum operational temperature), have considerable refrigeration requirements and thus become unattractive for continuous-duty operation. For intermittent use, they may be competitive.

- (b) With regard to field enhancement, Tables I and II illustrate the field contribution due to the iron return yoke. The magnet configuration is considered to be open-structured, as seen in Fig. 6. In room-temperature magnets, the iron contribution to the field is about 27%; in superconducting magnets, only 17%.

Field patterns in high-field split-coil magnets are illustrated in Fig. 7. The iron yoke is shown without a window for beam entry. Using the iron yoke alone as a flux return passage, the central field was enhanced approximately 16.5%. The fringing field at Points B and C are 0.084 T and 0.046 T, respectively, which affects adversely only instrumentation around the magnet. Additional iron shields increased the central field at A from 5.96 T to 7.1 T, which is a gain of $\sim 19\%$! The fringing field is reduced to small values. (The overall magnet current density in the coil $\lambda J = 2.5 \times 10^7$ A/m².)

In Fig. 8, the field homogeneity is shown for the above magnet. The homogeneity improvement is obvious in the magnet configuration with iron return yoke and additional shields. It may be pointed out that the iron yoke is assumed to be axially symmetric without any windows, perturbations due to bolts, etc. However, measurements with this magnet used with the SLAC bubble chamber, having a central field of 2.6 T, indicate that the field inhomogeneity over $X = \pm 0.25$ m and $R = \pm 0.5$ m was better than $\pm 1.5\%$.

Table I

Technical data and cost comparison of a water-cooled split-coil
arrangement with and without iron return yokes

	Copper coil, no iron	Copper coil, with iron	Aluminum coil, no iron	Aluminum coil, with iron
Central field (T)	2.6	2.6	2.6	2.6
a_1 (m)	0.7	0.7	0.7	0.7
α	2.2	1.95	3.2	2.5
β_1	1.471	1.171	1.471	1.371
β_2	0.271	0.271	0.271	0.271
λJ (A/m ²)	5.68×10^6	5.3×10^6	2.9×10^6	3.06×10^6
P (MW)	7.2	4.8	10.3	6
W_{coil} (kg)	57.8×10^3	32×10^3	41.6×10^3	33.6×10^3
W_{Fe} (kg) ⁽¹⁾	-	135×10^3	-	199×10^3
B_{coil} (T)	2.6	1.9	2.6	1.88
B_{Fe} (T)	-	0.7	-	0.72
<u>Cost in US dollars of:</u>				
Coil	3.82×10^5 ⁽²⁾	2.11×10^5	1.87×10^5 ⁽³⁾	1.51×10^5
Iron	-	1.49×10^5 ⁽⁴⁾	-	2.19×10^5
Power supply	3.6×10^5	2.4×10^5	4.84×10^5	3.0×10^5
Safety, Instrumentation	0.5×10^5	0.5×10^5	0.5×10^5	0.5×10^5
Support	0.3×10^5	0.3×10^5	0.3×10^5	0.35×10^5
Design, Engineering, Installation	0.7×10^5	0.7×10^5	0.7×10^5	0.7×10^5
Miscellaneous	0.6×10^5	0.5×10^5	0.6×10^5	0.6×10^5
TOTAL (US dollars)	9.52×10^5	8×10^5	8.81×10^5	8.85×10^5

(1) The iron thickness is 0.5 m.

(2) The present price of a copper coil, insulated and wound, including coil from fixtures, etc., is approximately \$6.00/kg. The price of extruded copper conductor is \$2.20/kg.

(3) The present price of an aluminum coil, wound, is \$4.50/kg. The price of extruded aluminum conductor is \$1.65/kg.

(4) The price of low-carbon steel, machined at matching surfaces, is estimated at \$1.10/kg.

Table II

Technical data and cost comparison
of a cryogenic and superconducting split-coil arrangement
with iron return yokes

	Aluminum coil, $r = 400^{(1)}$	Copper coil, $r = 176^{(1)}$	Superconducting coil with constant overall current density	Superconducting coil with current optimization
Central field (T)	2.6	2.6	2.6	2.6
a_1 (m)	0.75	0.75	0.75	0.75
α	1.8	2	1.2	1.2
β_1	1.293	1.293	0.663	0.68
β_2	0.293	0.293	0.293	0.293
λJ (A/m ²)	5.9×10^6	4.8×10^6	4.2×10^7	-
P (kW)	18	22	-	-
W_{coil} (kg)	15.4×10^3	70×10^3	2×10^3	21×10^3
W_{Fe} (kg)	190×10^3	210×10^3	110×10^3	110×10^3
B_{coil} (T)	2.1	2.1	2.15	2.15
B_{Fe} (T)	0.5	0.5	0.45	0.45
<u>Cost in US dollars of:</u>				
Coil	$3.6 \times 10^{5(2)}$	4.6×10^5	2.8×10^5	2.3×10^5
Iron	2.1×10^5	2.3×10^5	1.15×10^5	1.15×10^5
Cryostat	0.3×10^5	0.3×10^5	0.25×10^5	0.25×10^5
Power supply, Instrumentation	-	-	0.2×10^5	0.2×10^5
Refrigerator	6.5×10^5	7×10^5	1.3×10^5	1.3×10^5
Coil support	0.5×10^5	0.4×10^5	0.4×10^5	0.4×10^5
Vacuum system	0.5×10^5	0.5×10^5	0.5×10^5	0.5×10^5
Design, Engineering, Installation	1.4×10^5	1.4×10^5	1.8×10^5	1.8×10^5
Miscellaneous	1×10^5	1×10^5	1×10^5	1×10^5
TOTAL (US dollars)	15.9×10^5	17.5×10^5	9.4×10^5	8.9×10^5

(1) r is expressed in terms of $\rho_{300}/\rho_{21^\circ\text{K}}$. Magnetoresistance, mechanical strain, thermal contraction forces, influence of thermal and magnetic cycling are taken into account.

(2) Price of the pure aluminum strip is estimated at \$25/kg.

(3) Cost of power supply is ~ \$3000 - \$5000 and is included in the Miscellaneous figure.

V. BEAM TRANSPORT MAGNETS

To compare field distribution of beam transport magnets with and without iron return yokes, we used the field equations given in Section II, as well as results of the SLAC Computer Code NUTCRACKER. It may be recalled that the SLAC code utilizes only square mesh configuration. Although a program is written which simulates the coil and core contours fairly accurately to any desired shape, results in the border area close to the inner coil radius are not accurate.

The quadrupole magnets studied are shown in Fig. 9 (a - h). The coils are assumed to be symmetrical and obey the 2/3 rule. The current density in all coils is 1.7×10^8 A/m² and constant. The coil inner diameter is also kept constant at $2a_1 = 0.2$ m. The gradient distribution over X and Y is illustrated in Fig. 9.

For shell-type quadrupoles with cylindrical iron yokes, the maximum field gradient of

$$G(0) = \frac{\mu_0 \lambda J}{\pi} \left\{ \sqrt{3} \ln \alpha + \frac{1}{2} \left(\frac{a_1}{b_1} \right)^4 \cdot [\alpha^4 - 1] \right\} \quad (26)$$

gives good fourth-order results compared to the results obtained from variable iron permeability calculation. If iron is in the proximity of the coil ($b_1 = a_2$), the iron influence improves field homogeneity. However, in superconducting magnets, it is not desirable to cool the iron return yoke to cryogenic temperature and thus the iron inner diameter is, in general, much larger than the coil outer diameter ($b_1 > a_1$) to accommodate dewars and vacuum tanks. For Panofsky-type quadrupoles, the equation

$$G(0)_{\max} = \frac{2\mu_0 \lambda J}{\pi} \left\{ \tan^{-1} \frac{1-t^2}{2t} - \tan^{-1} \frac{\alpha^2 - t^2}{2\alpha t} + \frac{1}{2} \left(\frac{a_1}{b_1} \right)^4 [\alpha^4 - 1] \right\} \quad (27)$$

yields results with $\sim 5\%$ of data obtained from variable μ computer outputs. In this equation, $t = l/a$, the ratio of the coil height to the aperture width, and $\alpha = a_2/a_1$. The iron dimension is chosen such that ample space is provided for dewars, vacuum tanks, or other auxiliary parts required for cryogenic and superconducting magnets. The field in quadrupoles with iron in proximity of the coil had a value of ~ 7 T at $r = b_1$. The iron outer dimensions are determined from the field distribution within the iron. If the field in the iron at b_2 is approximately 0.6 T, the fringing field in air around the iron will be less than 0.1 T.

The field distribution in iron ($B_{x,y} = [B_x^2 + B_y^2]^{1/2}$) is illustrated in Fig. 10. For this particular quadrupole, lines of constant $\Delta G/G_{00}$ within the coil aperture are given in Fig. 11.

The next set of data is given for quadrupoles composed of two intersecting ellipses, with $2b$ as the major and a as the minor diameter. The field gradient

$$G(0) = \frac{\partial B_Y}{\partial X} = \mu_0 \lambda J \frac{a - b}{a + b} \quad (28)$$

is for the particular case studied in Fig. 12 and equal to $G = 40$ T/m with the maximum field at the conductor $B_Y = 6$ T. The current density in the coil is $\lambda J = 10^8$ A/m², with $a = -0.15$ m and $b = 0.29$ m.

For calculation purposes, the coil contour is approximated by 12 straight lines such that Eq. (4) is applicable. The number of straight lines was selected such that the calculation error everywhere in the aperture is smaller than 10^{-3} . To illustrate

the effect of perturbations, we assume that only one coil segment (out of 4) is shifted in the Y direction by 10^{-3} m. The effect of this perturbation is shown in Fig. 13. Compared to the ideal case, the region of 0.1% homogeneity is reduced in the first quadrant.

If, again, one coil section is moved by 10^{-3} m in the X direction, the field pattern according to Fig. 14 is obtained. These perturbations introduced in our coils are small. In practice, winding and assembling of coils may result in much larger coil asymmetries which affect the region of $\Delta G/G_{00} \leq 10^{-3}$ quite drastically. In Fig. 15, we illustrate the practical case that at the intersection of the two ellipses, the conductor has been removed. Also a gap of 2×10^{-3} m is assumed between the coils and directly adjacent to the X and Y axes. The G distribution can be compared to the ideal case given in Fig. 10. To correct for the perturbations shown in Fig. 16, we use a 12-pole coil with conductors parallel to the Z axis. The current passing through each conductor is 2.6×10^3 A (0.31% of the total coil MMF) if a 12-pole configuration is chosen, or 3.6×10^3 A (0.72% of the total coil MMF) if a 20-pole configuration is preferred.

To study dipole coils and the effect of perturbations, we have selected the well-known case of intersecting circles. If c denotes the distance between the centers of the two intersecting circles of radius a , the field inside the useful aperture is given by

$$B_Y = \frac{\mu_0}{2} \cdot c \cdot \lambda J$$

$$B_X = 0$$
(29)

For a current density $\lambda J = 10^8$ A/m², $a = 0.198$ m, $c = 0.096$ m, we have a central field of $B_0 = 6$ T. The aperture diameter $d = 0.15$ m. In Fig. 17, the field contours for $\pm 0.1\%$ and $\pm 0.5\%$ homogeneity are illustrated for the ideal case.

To illustrate the effect of ferromagnetic return yokes, we have chosen iron configurations shown in Fig. 18 (a - e). The ideal coil configuration is approximated by a step function, with $a_1 = 0.15$ m inner radius. The central field generated by a coil alone having a current density of $\lambda J = 10^8$ A/m² is $B_{00} = 6.14$ T. With the iron shield, a field of $B_{0,0} = 5.74$ T was produced at a current density of $\lambda J = 7 \times 10^7$ A/m². The average iron permeability is 113. Increasing the iron such that a better coupling between coil and return yoke is obtained, the field is increased to $B_{00} = 6.05$ T at the overall current density of $\lambda J = 7 \times 10^7$ A/m². Finally, by increasing the iron cross section even more, as seen in Fig. 18e, at $\lambda J = 7 \times 10^7$ A/m², a central field of 6.57 T with an average permeability of 140 was obtained. The $B = (B_X^2 + B_Y^2)^{1/2}$ distribution over the dipole coil and the field pattern in the iron return yokes is given in Fig. 19.

To illustrate the effect of perturbation, we chose the ideal coil configuration (intersecting circles) without iron return yoke and approximated the coil with a series of straight lines forming a polygon with 18 straight sections per coil quadrant. At $\lambda J = 10^8$ A/m², $B(0,0) = 6$ T. If the coil section A_1 is moved parallel to the Y axis by 2×10^{-3} m, forming a gap between the coil and the X axis, its field distribution is given in Fig. 20. If a gap of 2×10^{-3} m is formed between the A_1 section of coil and the Y axis, the field distribution is according to Fig. 21.

If in all four coil sections a segment with a height of 3.2×10^{-3} m is cut out and in addition, a gap of 2×10^{-3} m is left between the coil and the X axis, a field distribution according to Fig. 22 is obtained. To correct the effect of perturbations, a number of filamentary conductors parallel to the Z axis were placed at the coil in the diameter.

To give an order of magnitude of correction by choosing a sextupole configuration, the current of 4.1×10^3 A per current line (0.33% of the total coil MMF) is necessary

to produce the correction given in Fig. 23. If a 10-pole correction is selected, a current of 4.23×10^3 A per current line is required, which corresponds to 0.57% of the total coil MMF.

VI. HIGH-HOMOGENEITY MAGNETS

It was shown that iron improves two-dimensional field homogeneity in uniformly shielded, axially-symmetric, and beam transport magnets. For these magnets, requirements on homogeneity are not stringent. The experiment may require a homogeneity of 10^{-3} over the useful magnet aperture, which is not difficult to achieve, if deviation from the ideal coil configuration can be kept to a minimum (conductor tolerances, dimensional stability, symmetrical coil arrangements).

However, problems become more complex when full accessibility to the aperture from one or more directions is required. In 6th- and 8th-order coils, where field homogeneities in the order of 10^{-5} are required over a certain space to accommodate the experimental setup, the choice of iron, its shape and thickness, must be made with more care.

While the direct field calculation in coils without iron does not pose any problem, the presence of iron shields around the coils introduces a number of errors in the accuracy of computational results. A few reasons are summarized below:

1. The variable permeability computation must converge to an error of at least 10^{-7} or less, if the data would be trustworthy. Single precision calculation used in the SLAC code yielded an error of $\sim 10^{-6}$ after 500 iterations. The error function oscillates and does not converge further. Double precision improved the situation, and an error of 10^{-7} was obtainable.
2. With the SLAC computer (360/91) a magnetostatic problem with 150×150 nodes or any combination not exceeding 2.25×10^4 nodes can be solved. Requiring double precision reduces the area to 100×100 meshpoints. If, in open-type magnets (with or without ferromagnetic shields), the potential boundaries ($A = 0$ or constant) are close to the magnet (say a ratio of the distance to the boundary to the magnet extension will be 1.5/1 or 2/1 in either direction), the computational errors are in the order of 10^{-2} to 5×10^{-3} . Contour plots for lines of constant $\Delta B/B$ or $\Delta G/G$ are distorted. In order to minimize the influence from border-lines, the magnet extensions must be at least one-fifth of the distance from the border-line, or image methods should be used.

To illustrate the difficulties, the example of an 8th-order axially-symmetric coil with a central field of 5 T and homogeneity of $\sim 10^{-5}$ over the area of 22×24 cm² is calculated. The coil geometry without an iron shield and contour lines of constant $\Delta B/B$ is given in Fig. 24. The coil system yields, in the area of interest, contours fairly close to the ideal dipole distribution. Field calculations for the same magnet with a ferromagnetic shield are given in Fig. 25. Direct comparison of calculations utilizing variable permeability programs with iron return yoke removed to the results obtained in Fig. 24 proved to be misleading. Field calculations utilizing difference equations used the position of boundaries with $A = 0$ or $A = \text{constant}$ at a finite distance from the magnet, while field calculations of coils without iron place the $A = 0$ boundary at infinity. The location of the boundary, dictated by the storage capacity of the computer, arbitrarily distorts the field contour pattern. The position of the line $\Delta B/B = 0$ shifted to the right (X direction). The computational error (using double precision) after 370 iterations was $\sim 2 \times 10^{-7}$. The mesh size chosen had the dimension of 1.676×1.676 cm². The magnet extension in the X direction from the symmetry axis was 29 meshpoints, while the boundary $A = 0$ was at node 100. The absolute value of $\Delta B/B$ is also changed from 8×10^{-5} to 3.5×10^{-4} within the 12×12 cm area, which is one-fourth of the area of interest. This is due to computational errors as well as

fitting the coil geometry into mesh units, which dictates accurate positioning of individual coils.

Placing the iron shield around the coils counteracts the effect of $A = 0$ boundary and changes the contour plot. The line of $\Delta B/B = 0$ is now shifted towards positive Y and the maximum value of $\Delta B/B$ is 2×10^{-3} in the area of interest. The main reason for the field distortion is due to the arbitrary choice of the iron thickness (~ 14 cm) and iron shape. The component of the flux density in the iron changed from 3.2 T at the symmetry axis to 1.9 T in the cylindrical part, and from 2 T to -0.5 T in the end plates. Optimum iron shaping is being attempted and seems promising.

An attempt to improve this deficiency is the following: The high homogeneity coil is calculated as a first approximation with large mesh sizes, such that the distances of the boundaries to the symmetry axes are at least 10 times the maximum coil extensions in both coordinates (x, y) or (r, θ) . For this case, lines of constant A are calculated. Double precision must be used. The problem must converge to errors of about 10^{-6} or smaller.

The magnet can now be subdivided into smaller mesh units. As the distance ratios between magnet dimensions and boundaries are changed (magnet grows in size within boundaries at fixed positions given by the size of the computer memory), the A boundaries, located at a new relative distance to the coil, must have the new values of A calculated at the first attempt with the larger mesh sizes. The relative error introduced by the finite field limitations is reduced due to this digitalization. However, in computer codes using square mesh, any subdivision into new mesh sizes will introduce geometrical errors, which either must be eliminated or corrected by means of current sheets.

VII. FIELD DISTORTION DUE TO COIL END EFFECTS

In beam transport and experimental magnets, the advantage of the high flux density (reducing magnet overall length) is somewhat counteracted by field distortion at the magnet entrance and exit due to coil end effects and the enhanced fringing field. The fringing field and the coil end effect influence field uniformity in the gap. Field corrections by means of correcting coils are complicated.

Field measurement in a wire chamber magnet with the bore dimensions of 2 m height, 3 m width, and 2 m depth, at a maximum field of 2 T showed that the deviation of $\int Bdl$ over the median plane in the uncorrected magnet exceeded 7%, and over the entire gap volume, 15%. Correcting the gap by appropriate pole shimming yielded a uniformity of $\int Bdl$ of 2% over 90% of the entire gap. As this result was not satisfactory, superconducting screens were used, which were placed between coil ends and the iron horizontal yokes to further improve $\int Bdl$ to 1%.

Calculations²³ with simplified coil end shapes indicate that for magnets without iron return yokes, coil end effects in quadrupoles influence two-dimensional field patterns within the gap to a depth of $2.5 a_1$ ($\Delta G/G \cong 10^{-3}$). In dipole coils, the end effects persist to a depth of $20 a_1$ ($\Delta B/B \cong 10^{-3}$).

The length of a dipole magnet without iron must be at least $40 a_1$ in order that the field homogeneity within the coil aperture, due to end sections, is 10^{-3} . This imposes a new constraint on the minimum magnet length, counteracting the high field advantage of the superconductor. Methods of end field correction need more investigation if high-field magnets are to become tools in high-energy physics research.

REFERENCES

1. D. DeKlerk, Newport Instruments Ltd. (1965).
2. J. H. Dorst, Proc. Int. Conf. on Magnet Technology, Stanford U., 182 (1965).
3. J. S. Colonias and J. H. Dorst, UCRL-16382 (1965).
4. A. M. Winslow, Journal of Computer Physics 1, 149 (1967).
5. R. Perin and S. Van der Meer, CERN 67-7, ISR Division (1967).
6. E. Burfine et al., SLAC-56 (1966).
7. R. A. Beth, Proc. 1968 Summer Study, Brookhaven National Laboratory, 842 (1968).
8. K. Halbach, UCRL-18947 (1969).
9. R. Yourd and K. Halbach, UCRL-18378 (1968).
10. J. Blewett, Proc. 1968 Summer Study, Brookhaven National Laboratory, 1042 (1968).
11. F. C. Trutt, Ph. D. Thesis, University of Delaware, Newark (1964).
12. E. A. Erdelyi et al., IEEE Trans. Power Apparatus and Systems, 792 (1966).
13. R. Perin, CERN Internal Report, ISR-MAG/66-8 (1966).
14. A. M. Winslow, UCRL-7784-T, Rev. 1 (1965).
15. A. Asner et al., Proc. Int. Conf. on Magnet Technology 3 (1967).
16. S. Caeymaex, Paper A40, Third Int. Conf. on Magnet Technology (1970).
17. A. A. Halacsy, Paper A87, Third Int. Conf. on Magnet Technology (1970).
18. E. Gerold, Stahl und Eisen, 613 (1931).
19. H. Brechna, Proc. Int. Conf. on Magnet Technology, 305 (1967).
20. T. Doke et al., Institute for Nuclear Study, University of Tokyo (to be published).
21. H. A. Danan et al., J. Appl. Phys. 39, 669 (1968).
22. L. B. Smith, SLAC-95 (1969).
23. J. Perot, SLAC-TN-69-20 (1969).

FIGURE CAPTIONS

1. Cross section of a conductor.
2. Current filaments for field corrections.
3. Conductor and iron configuration for quadrupole magnet.
4. Distribution of B_x over the iron yoke cross section.

1. $Y = 0, X$	$\theta = \pi/4$	(Fig. 9b)
2. $y = 0, x$	$\theta = 0$	(Fig. 9b)
3. $Y = 0, X$	$\theta = \pi/4$	(Fig. 9c)
4. $y = 0, x$	$\theta = 0$	(Fig. 9c)
5. $Y = 0, X$	$\theta = \pi/4$	(Fig. 9d)
6. $y = 0, x$	$\theta = 0$	(Fig. 9d)
5. Magnetization curves of low-carbon steel.
6. Axial symmetries, magnet lines of constant B.
7. Axially-symmetric magnet with iron yoke and shields.
8. Lines of constant $\Delta B/B$ for the magnet (Fig. 7).
9. $\Delta G/G_0$ curves for quadrupole arrangements given in (a - h).
10. Line of constant B for a quadrupole arrangement.
11. Contour lines of constant $\Delta G/G_{00}$ (quadrupole, Fig. 10).
12. Ideal quadrupole formed from two intersecting ellipses.
13. Quadrupole (Fig. 12) with one quadrant moved 0.1 cm in Y direction.
14. Quadrupole (Fig. 12) with one quadrant moved 0.1 cm in X direction.
15. Quadrupole (Fig. 12) with all quadrants moved.
16. Quadrupole (Fig. 15) with corrections by means of current filaments.
17. Ideal dipole configuration ($\lambda J = 10^8 \text{ A/m}^2$).
18. $\Delta B/B$ lines for dipole ($\lambda J = 10^8 \text{ A/m}^2$ core, $\lambda J = 7 \times 10^7 \text{ A/m}^2$ iron yoke) with iron return yokes.
19. Line of constant B for dipole (Fig. 18).
20. Dipole (Fig. 17) with section A_{11} shifted 0.2 cm in Y direction.
21. Dipole (Fig. 17) with one coil shifted 0.2 cm in X direction.
22. Dipole (Fig. 17) with both coils displaced.
23. Dipole (Fig. 17) with corrections (current filaments parallel to Z axis.)
24. Eighth-order coil without iron.
25. Eighth-order coil with and without iron return yoke (field computation with SLAC NUTCRACKER).

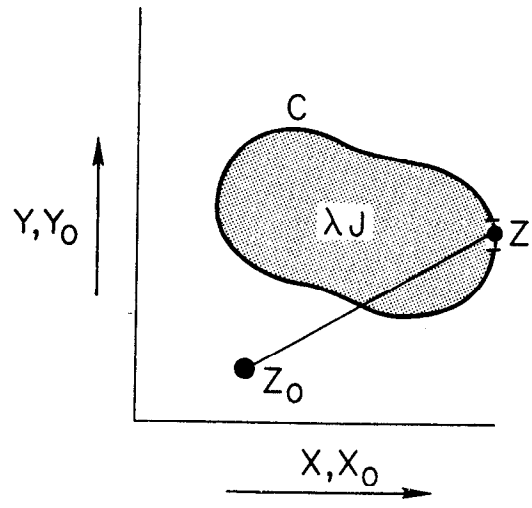


Fig. 1

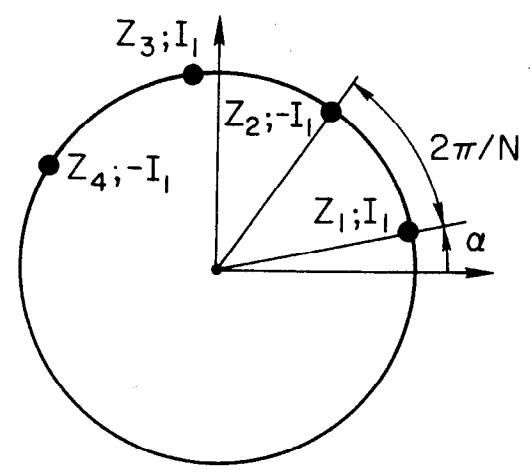


Fig. 2

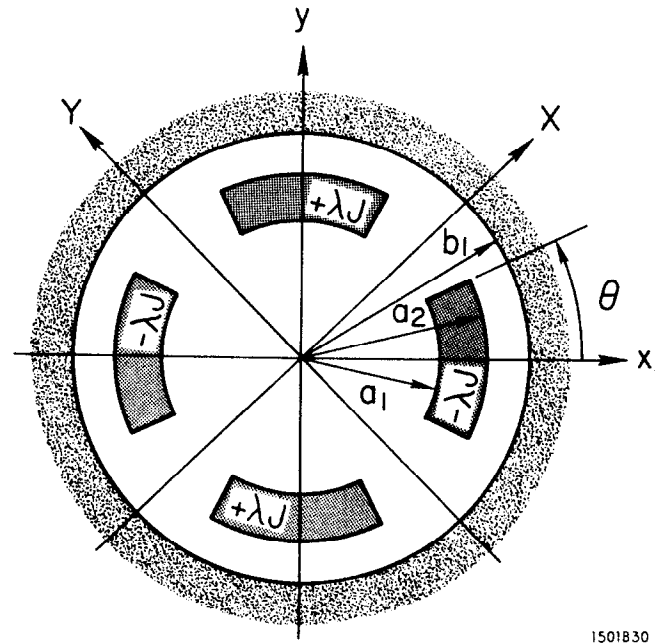
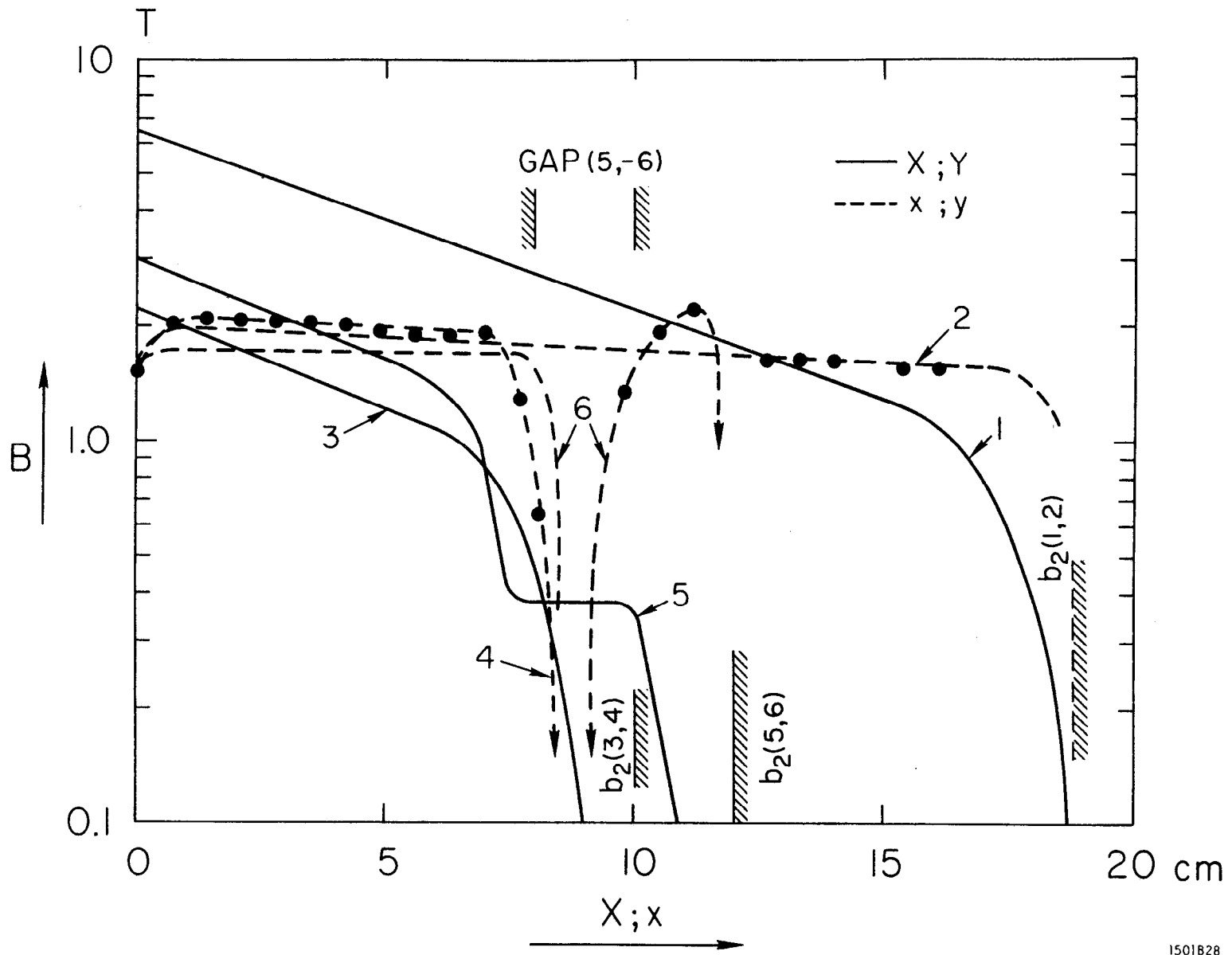
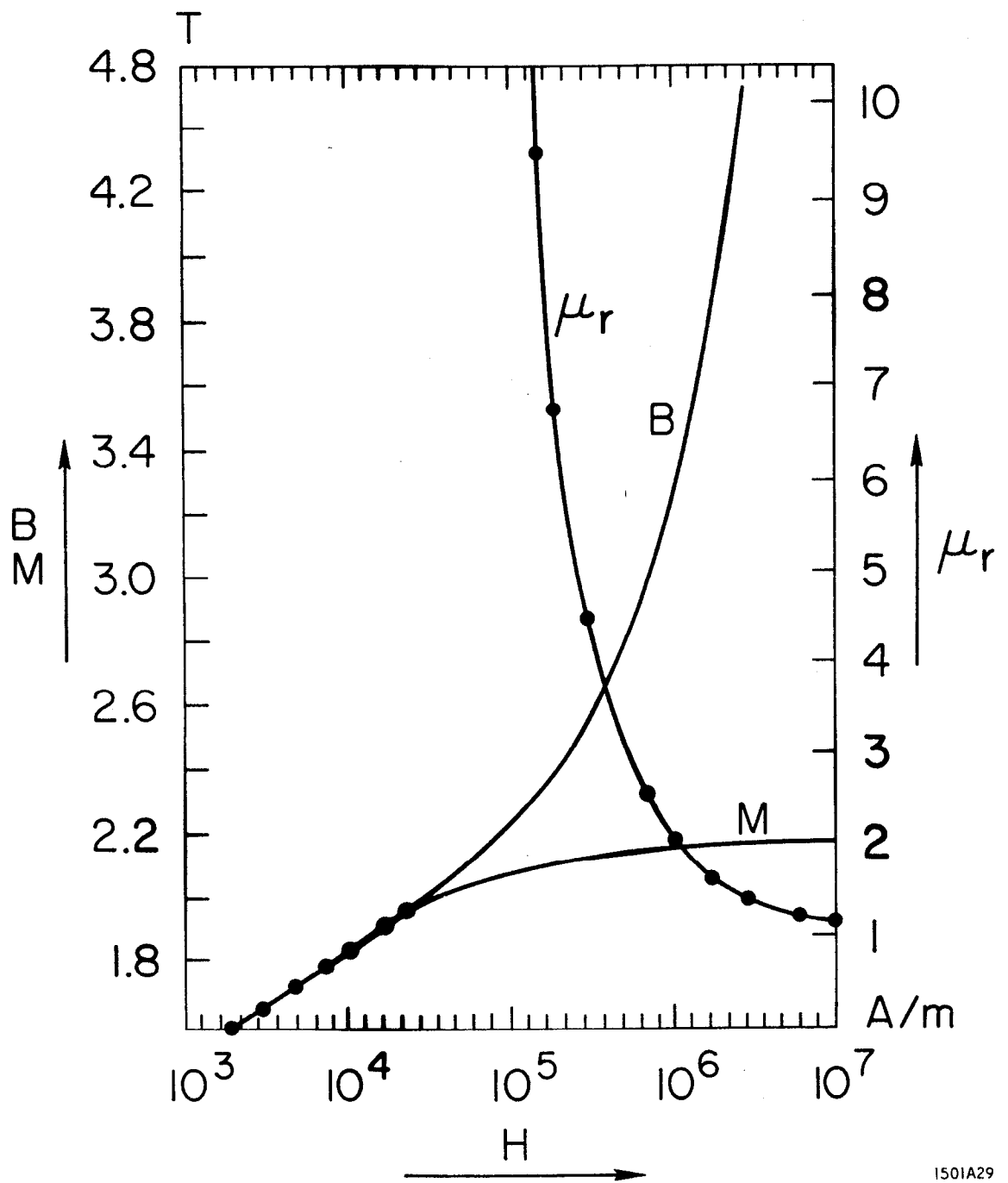


Fig. 3



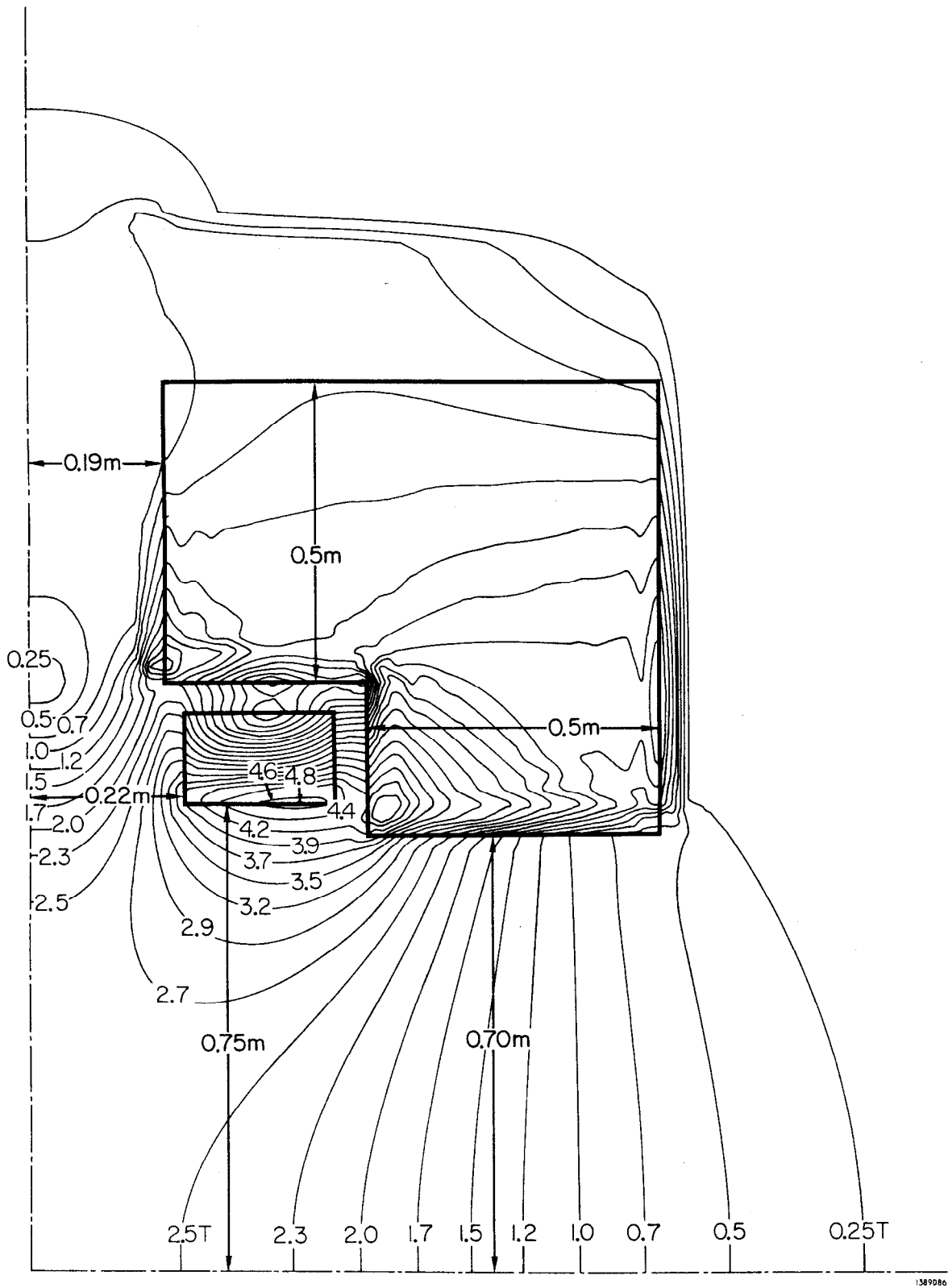
1501B28

Fig. 4



1501A29

Fig. 5



1389086

Fig. 6

Field at:	A(T)	B(T)	C(T)
Coil : No Iron, No Shields	5.96	0.25	0.17
Coil + Iron Yoke	6.96	0.084	0.046
Coil + Iron (Yoke and Shields)	7.1	0.018	0.010

BBI

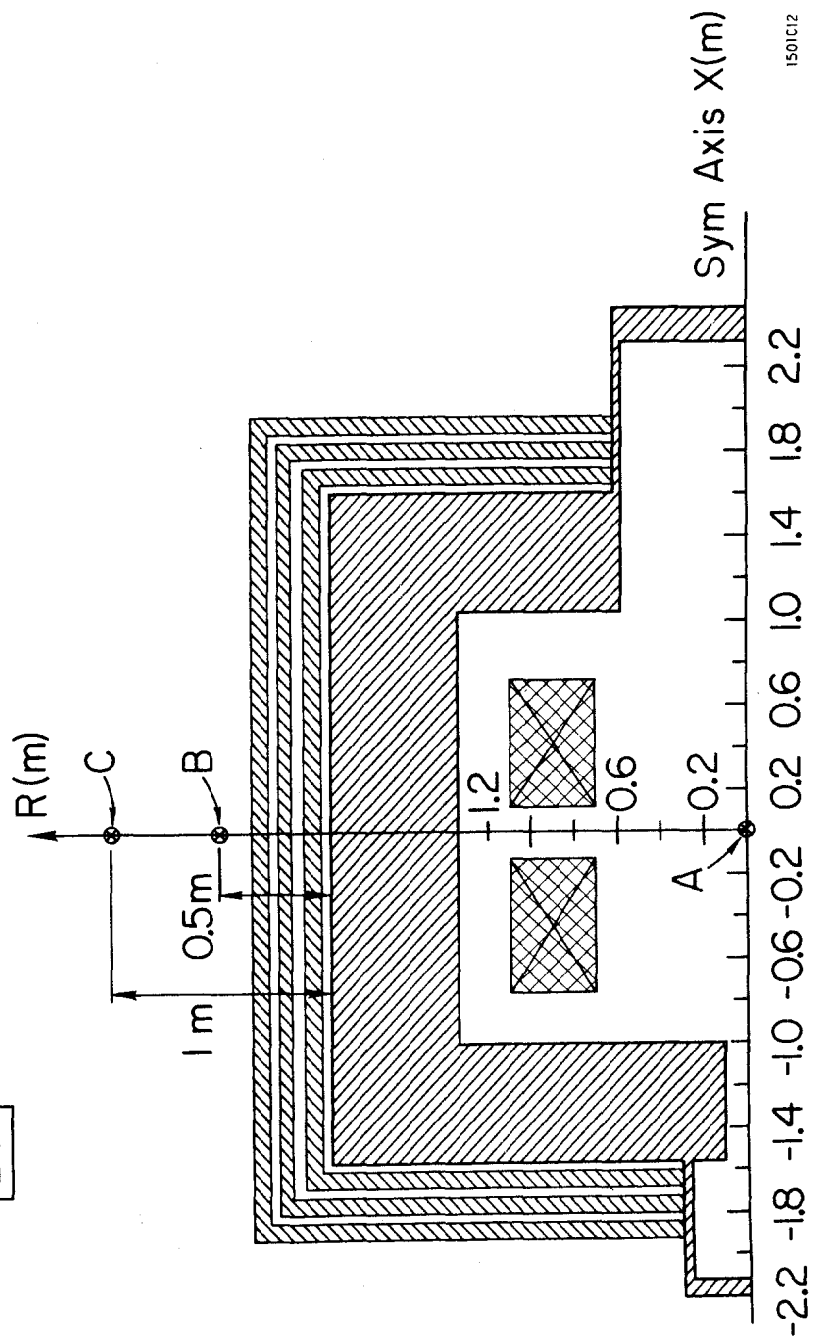


Fig. 7

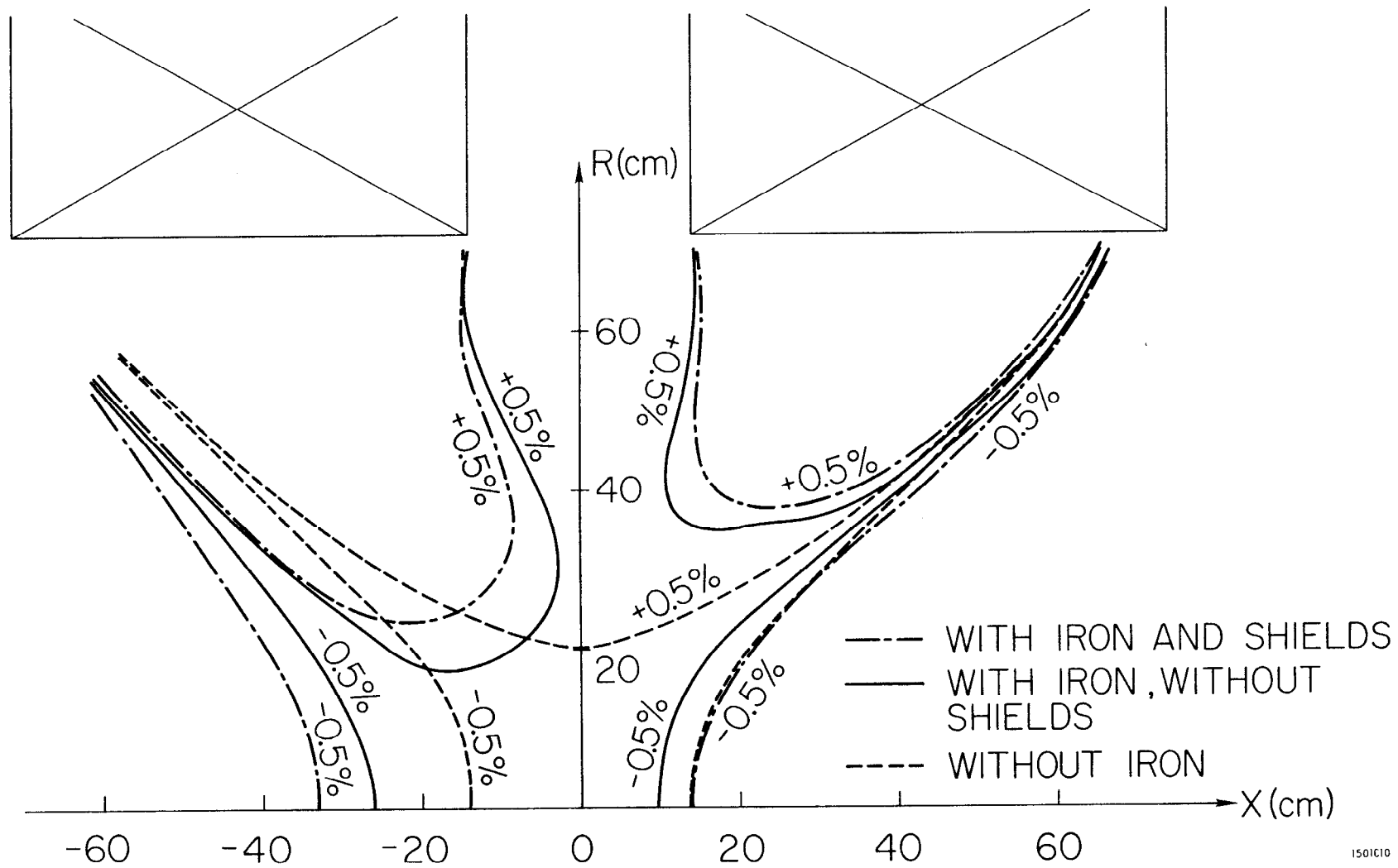


Fig. 8

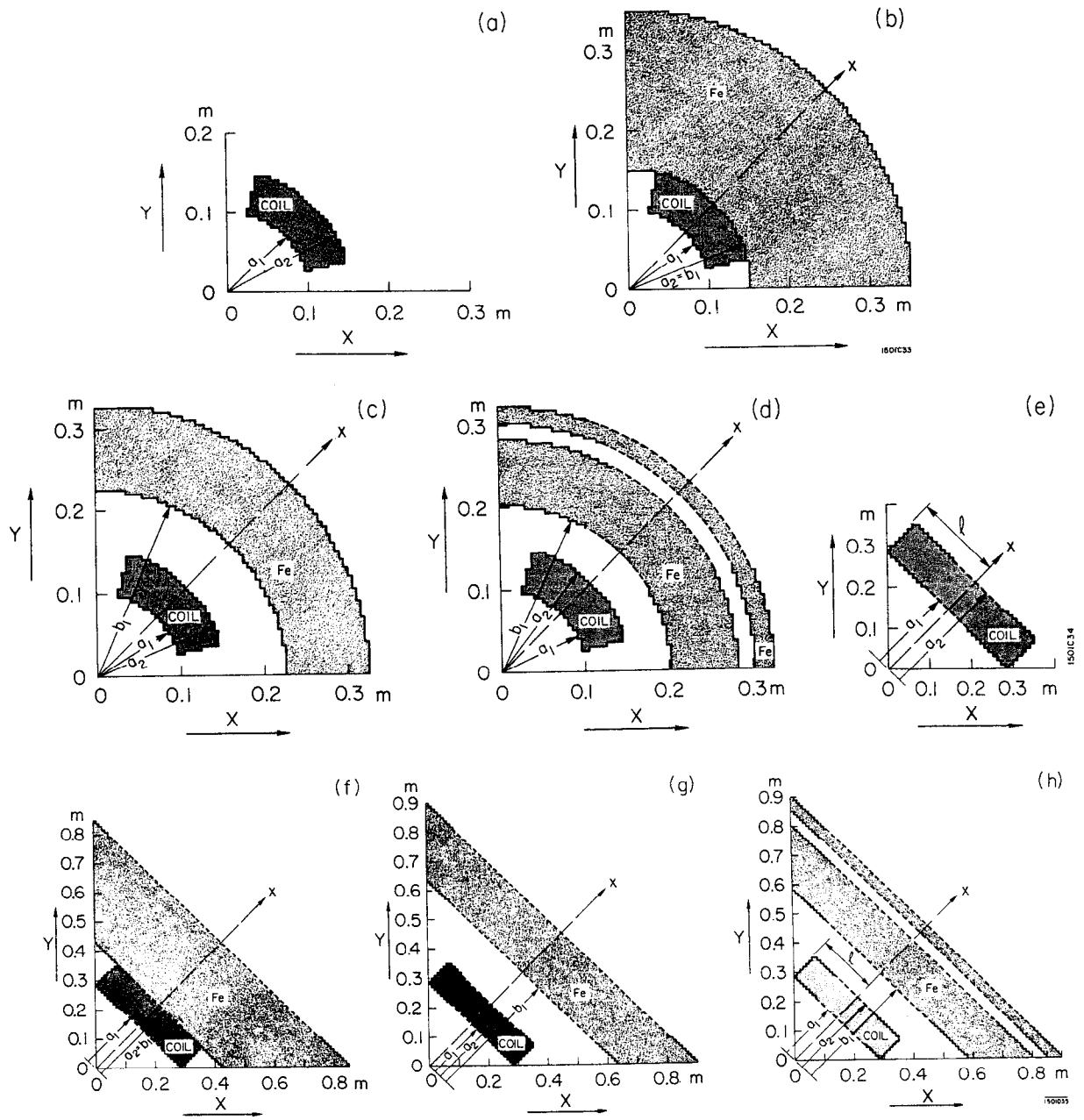
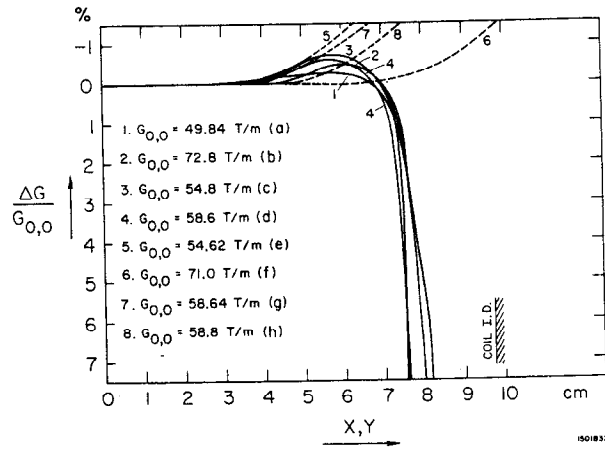
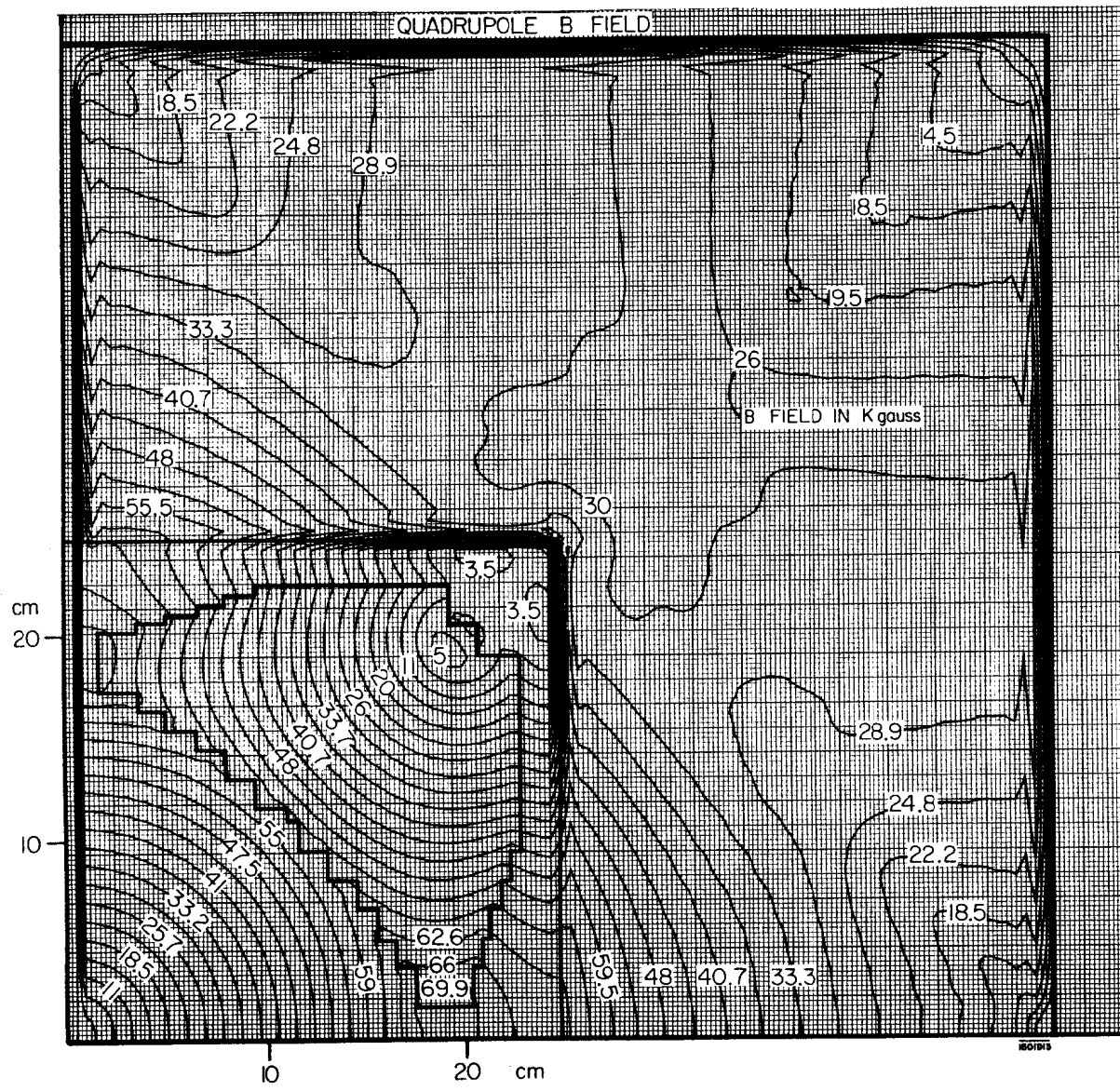


Fig. 9



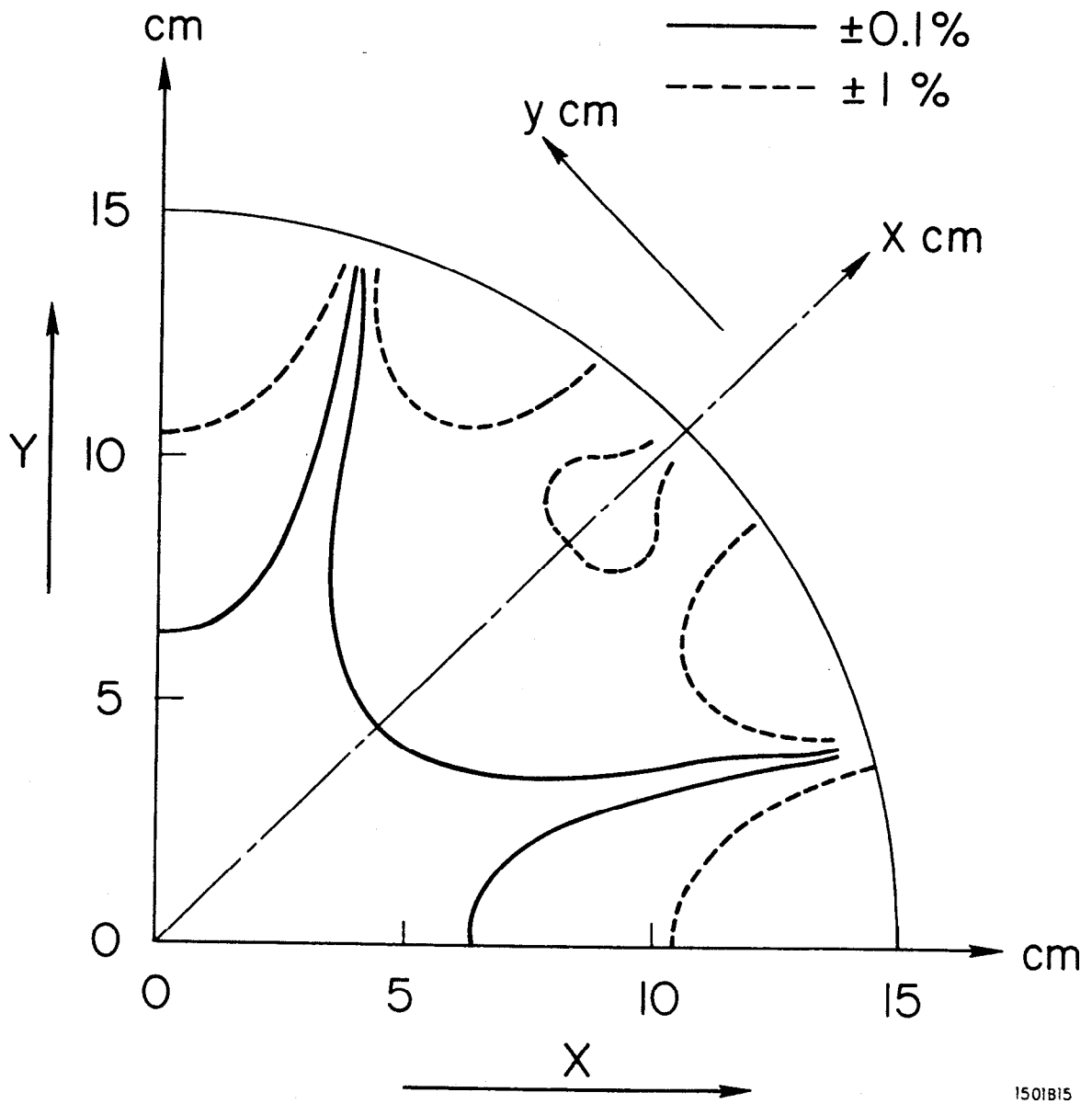


Fig. 11

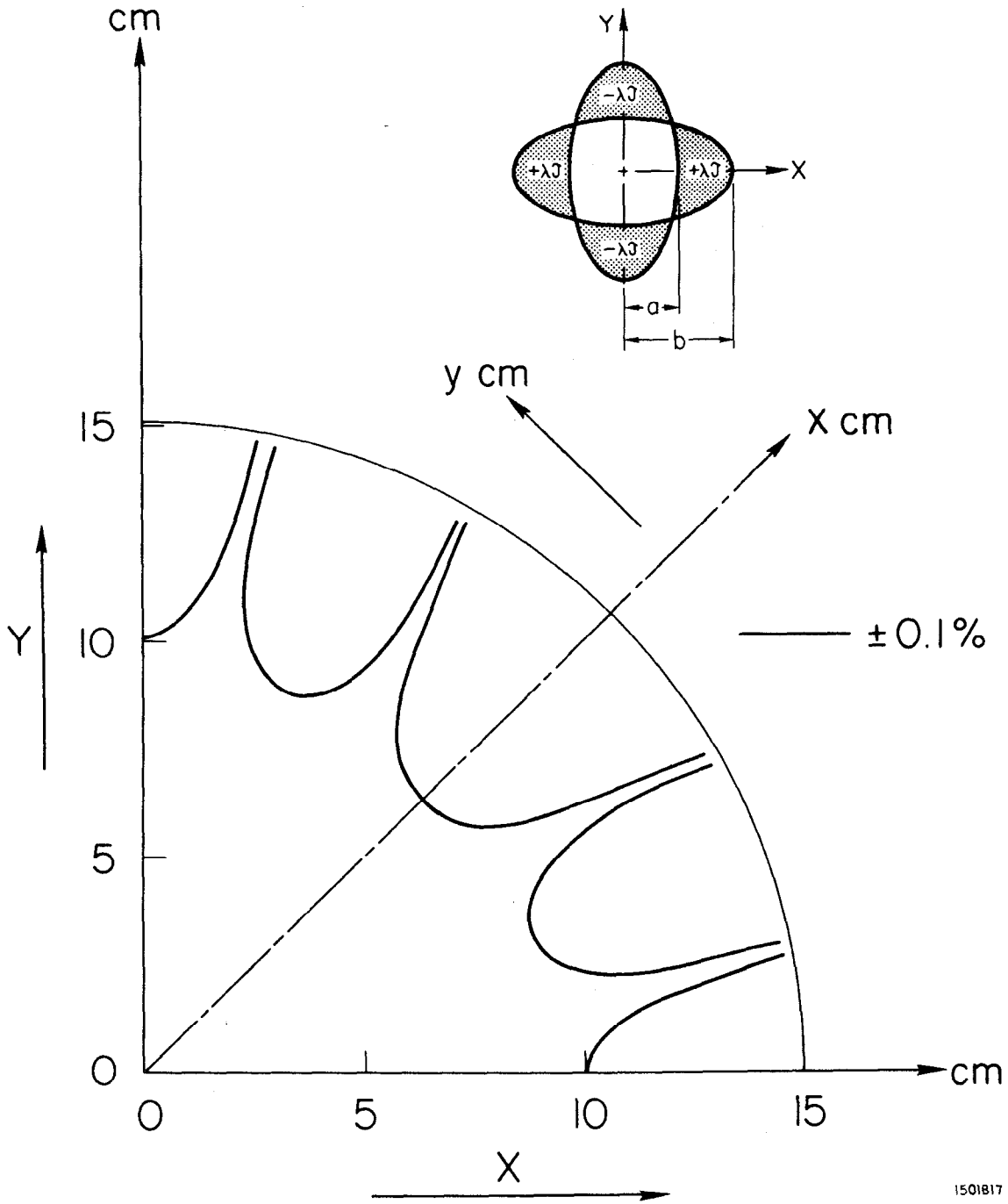


Fig. 12

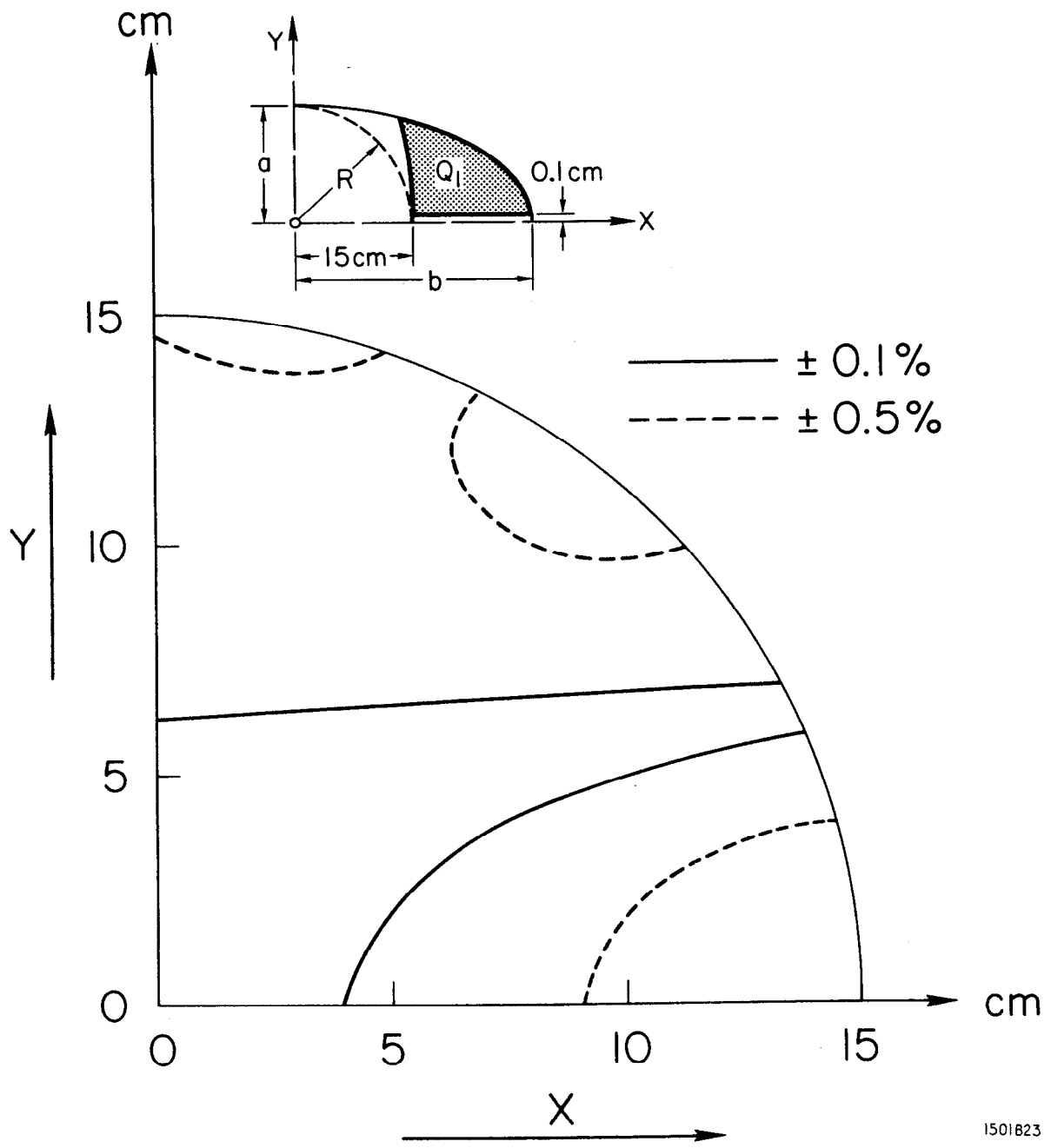
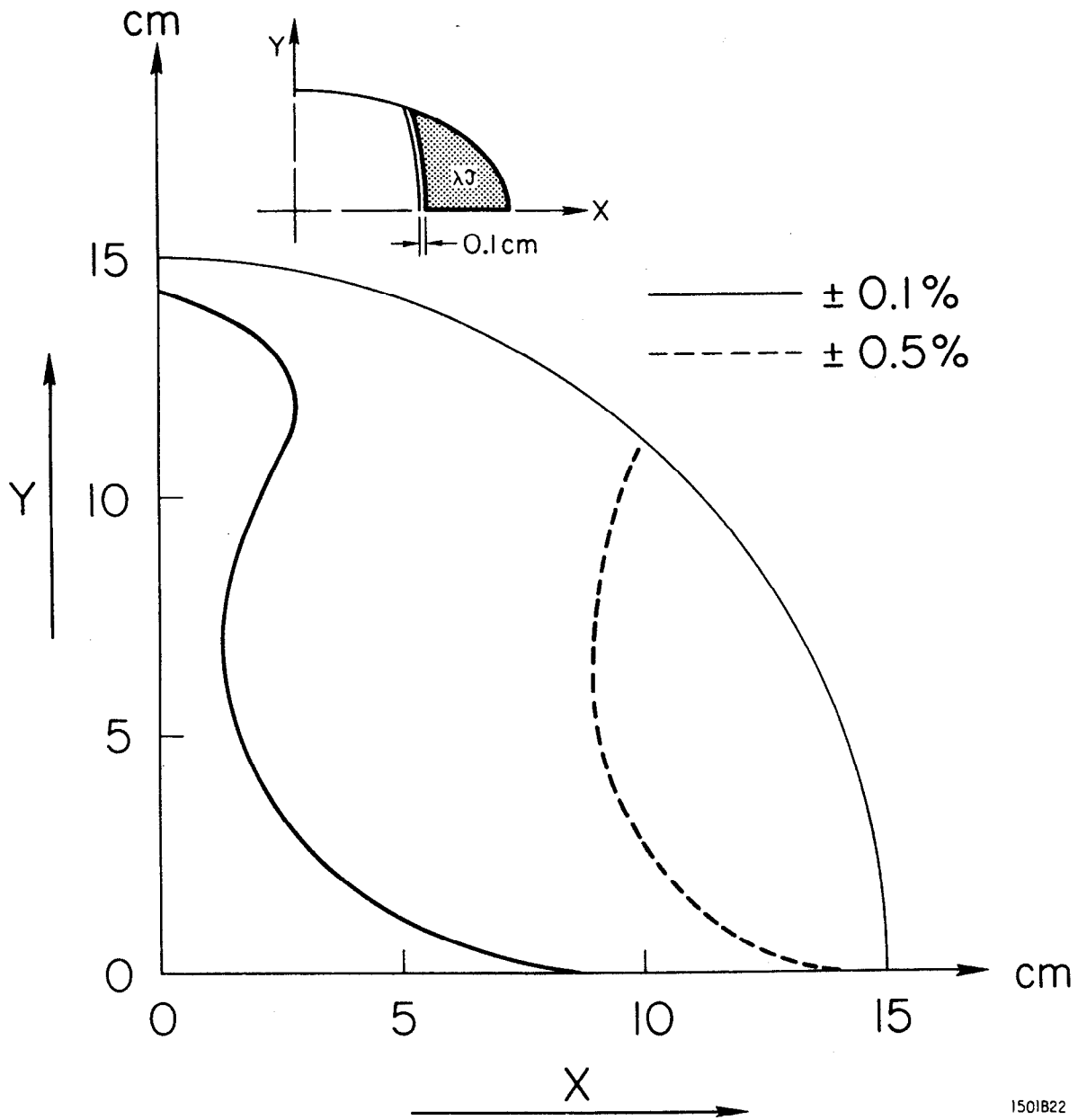
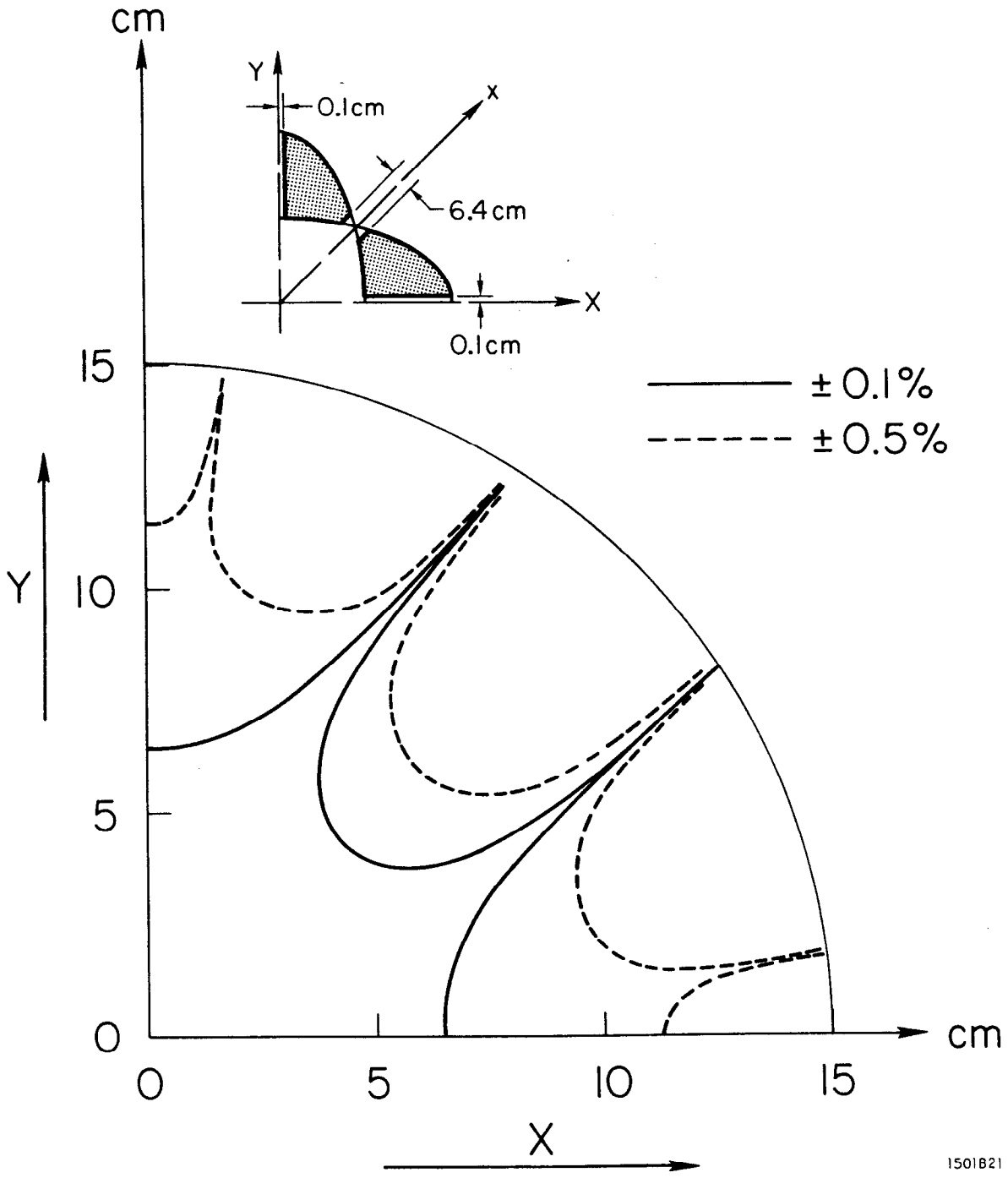


Fig. 13



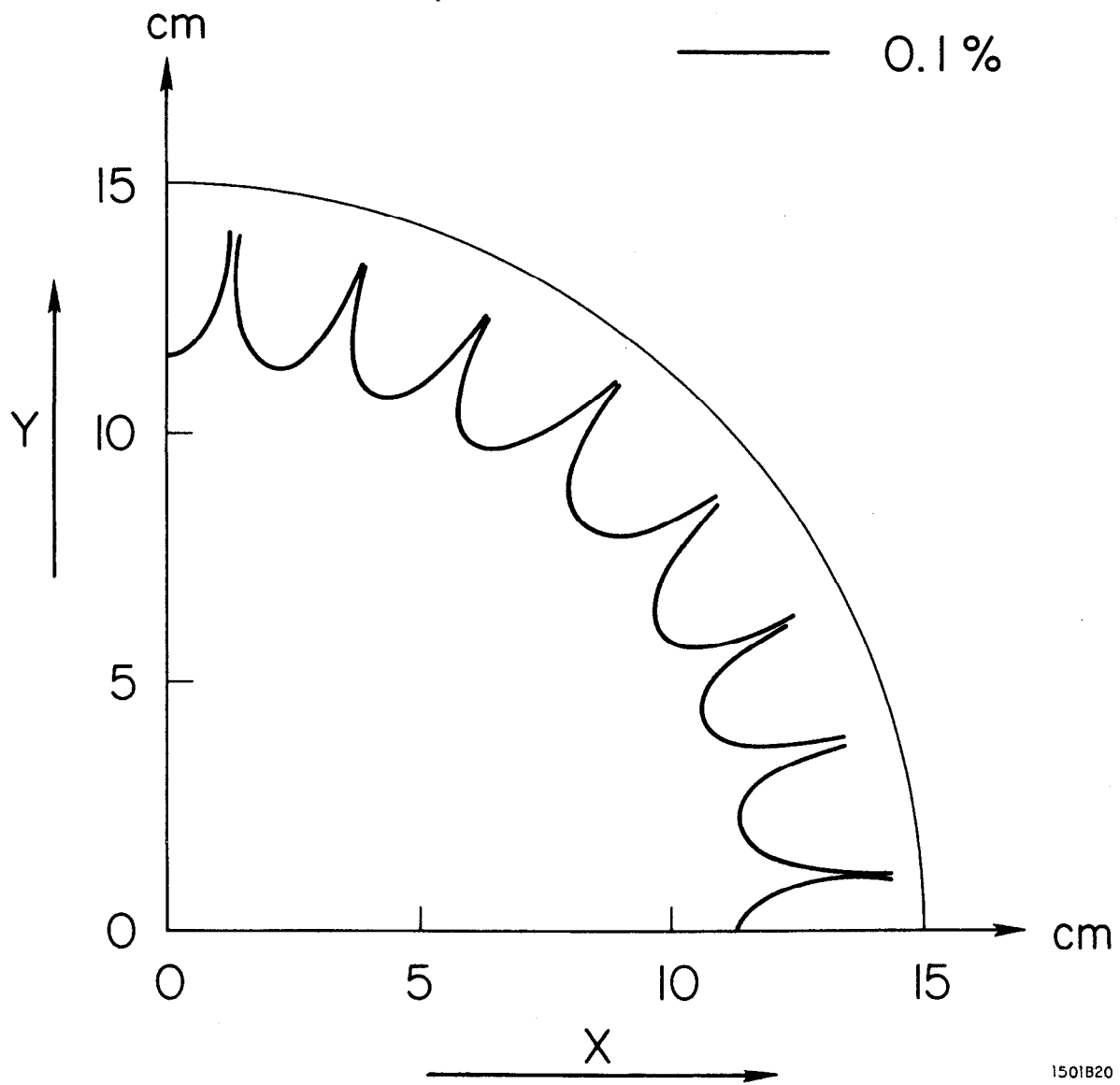
1501B22

Fig. 14



1501821

Fig. 15



1501B20

Fig. 16

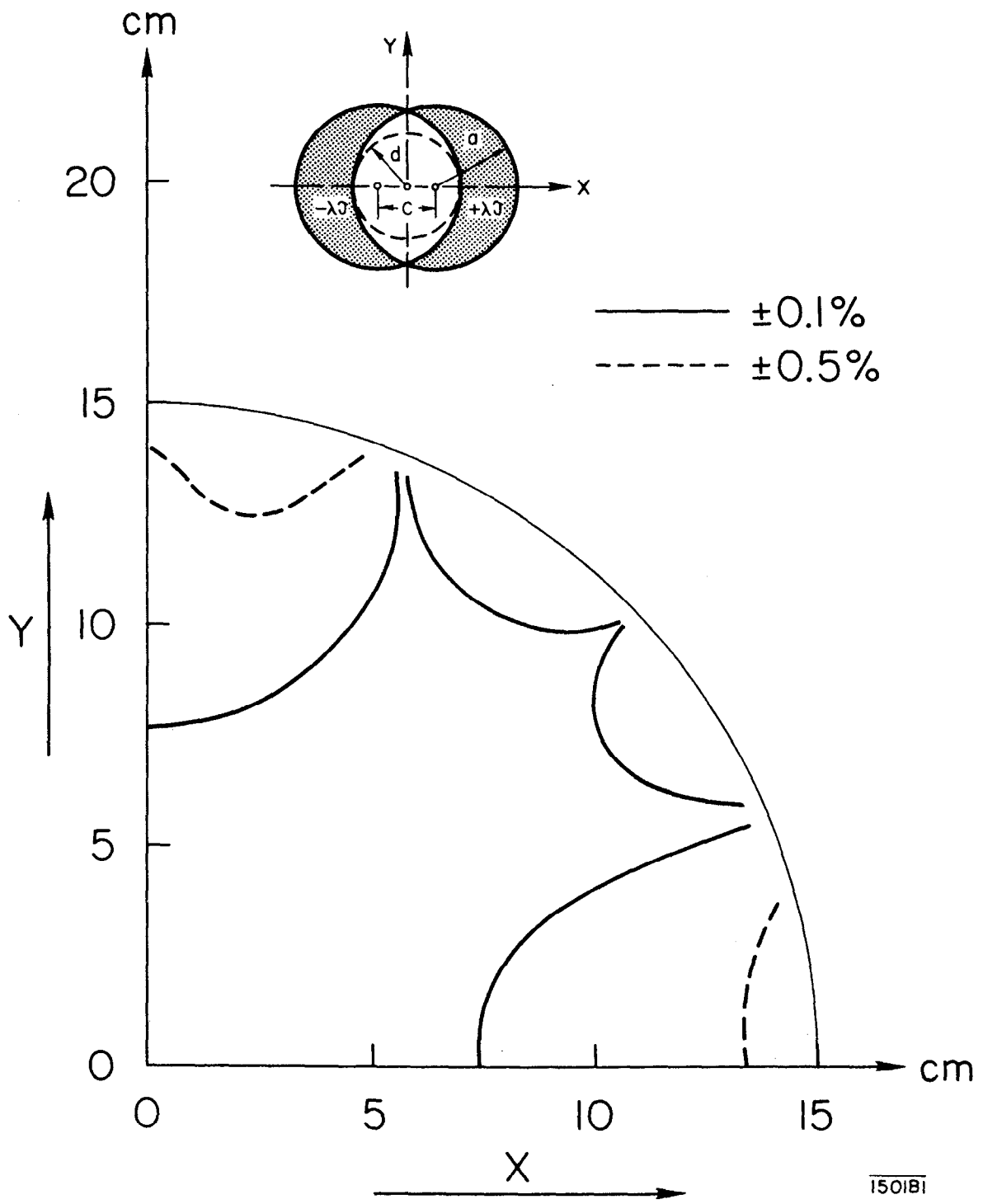


Fig. 17

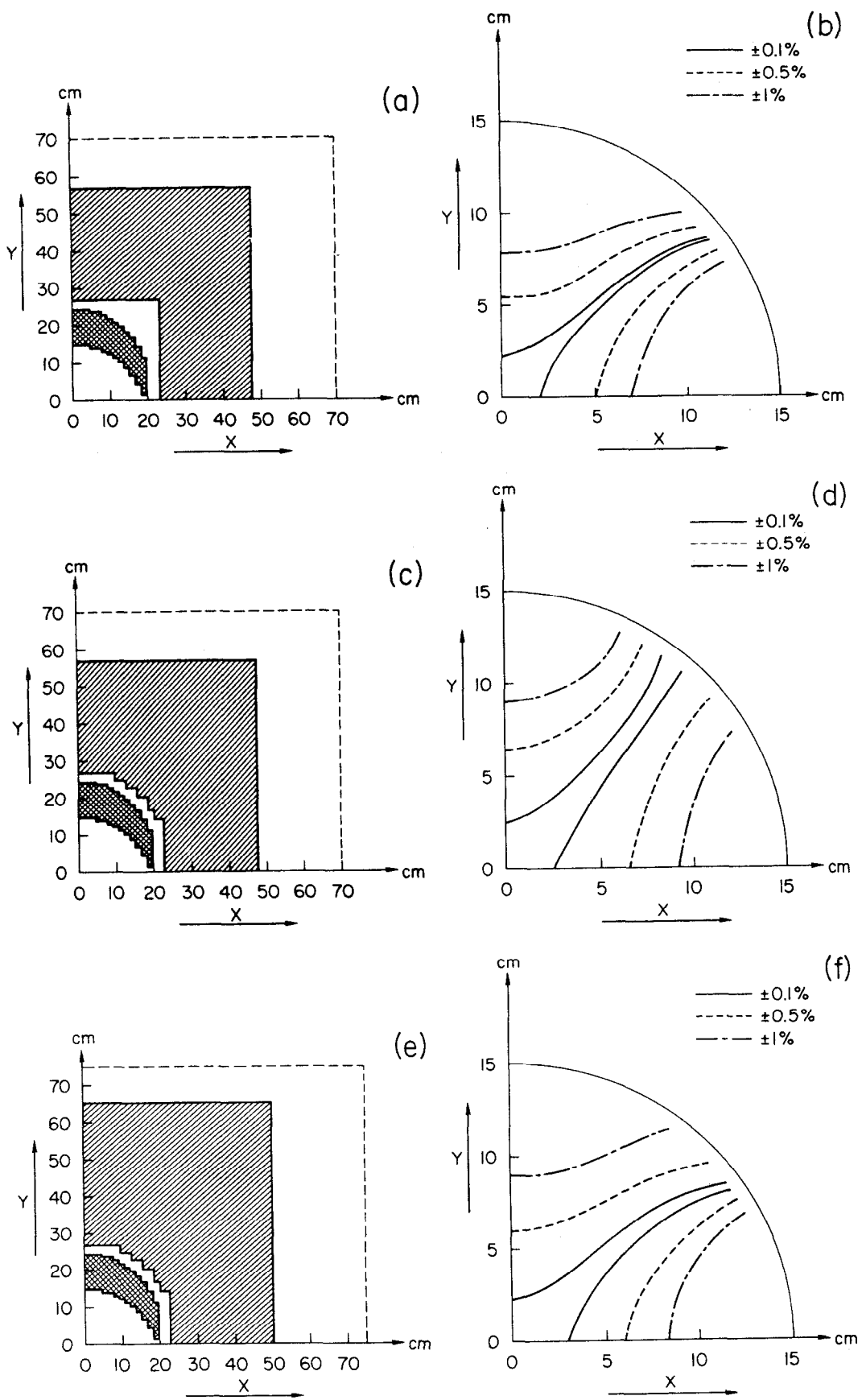


Fig. 18

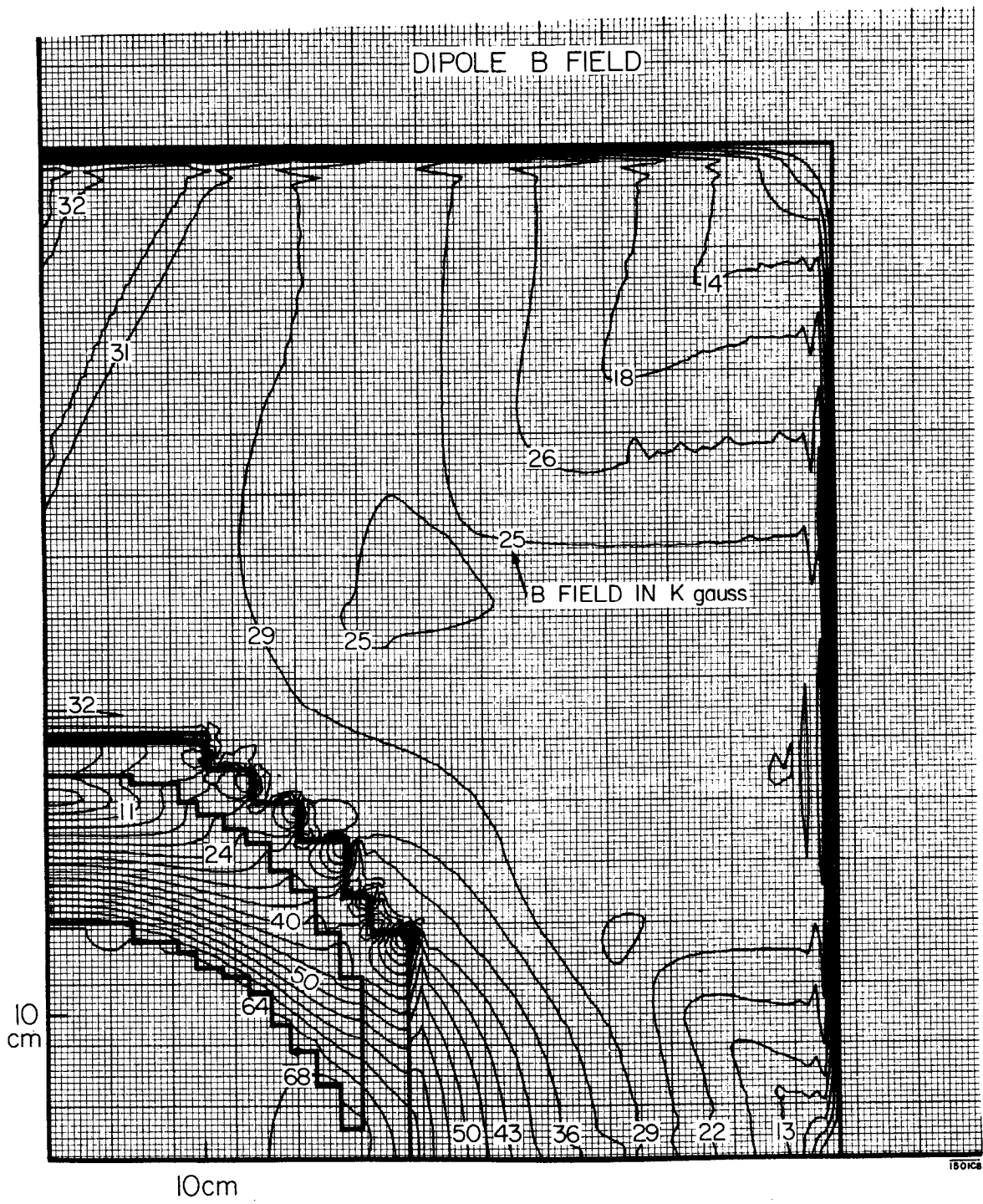


Fig. 19

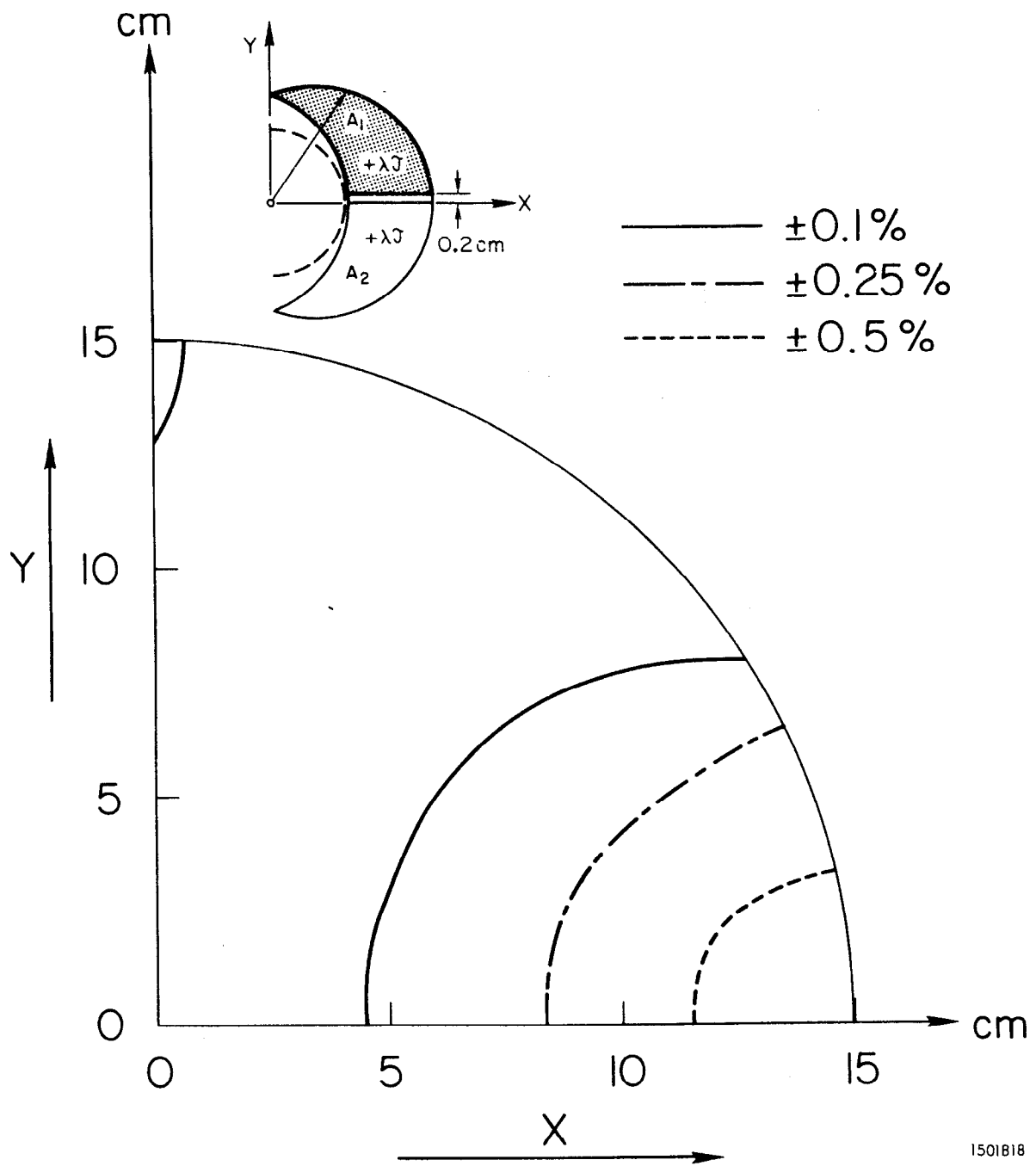


Fig. 20

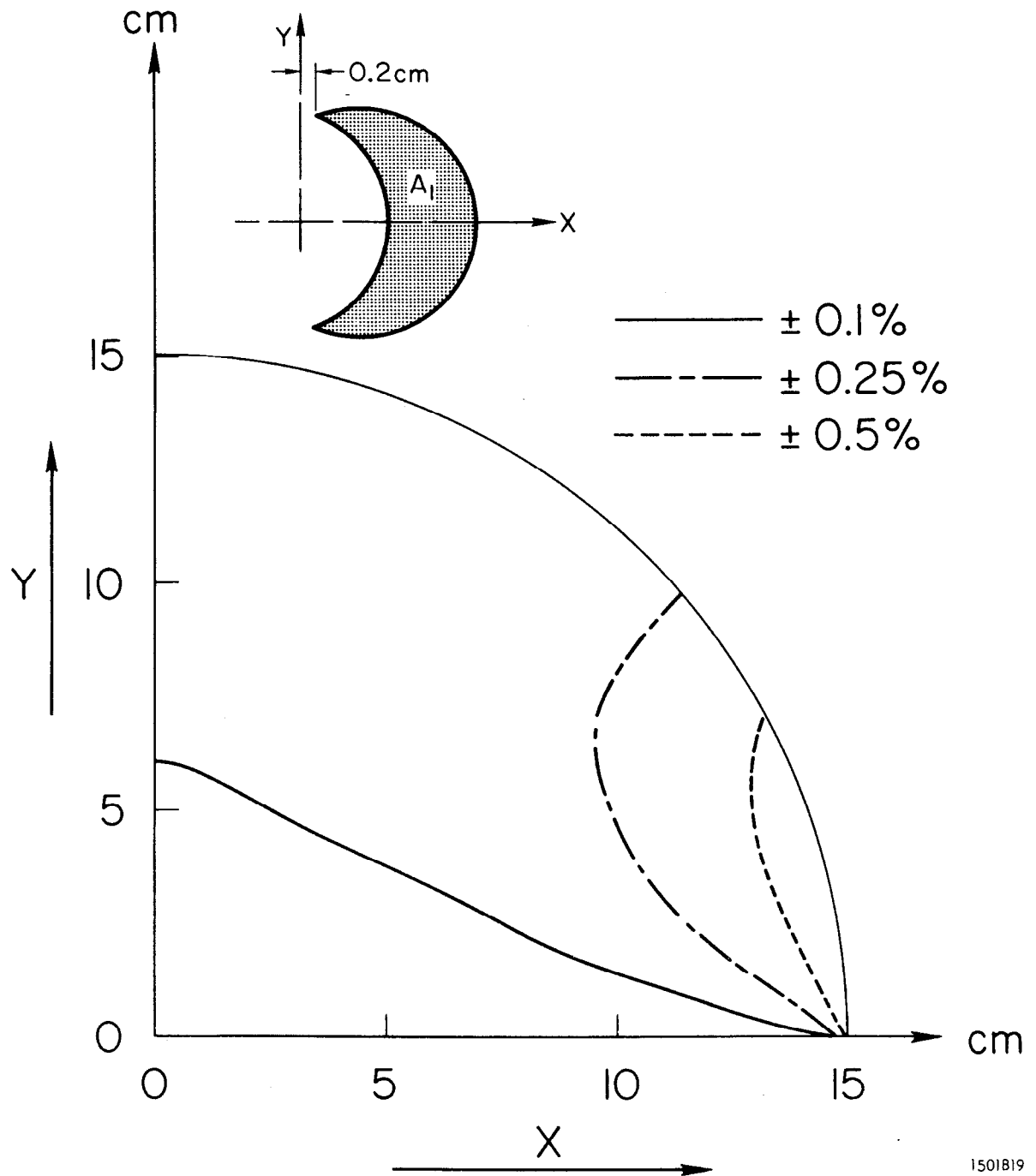
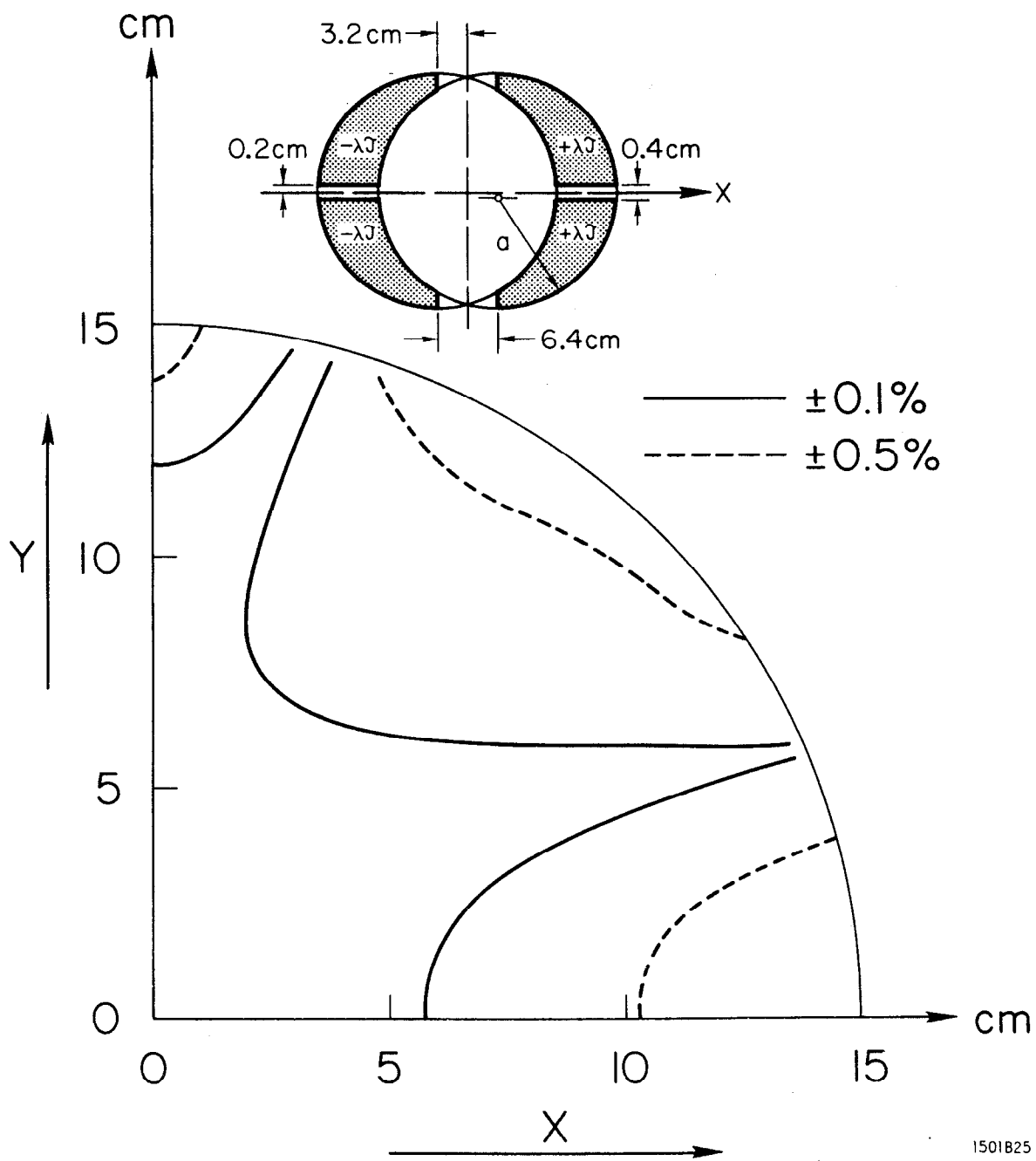


Fig. 21



1501B25

Fig. 22

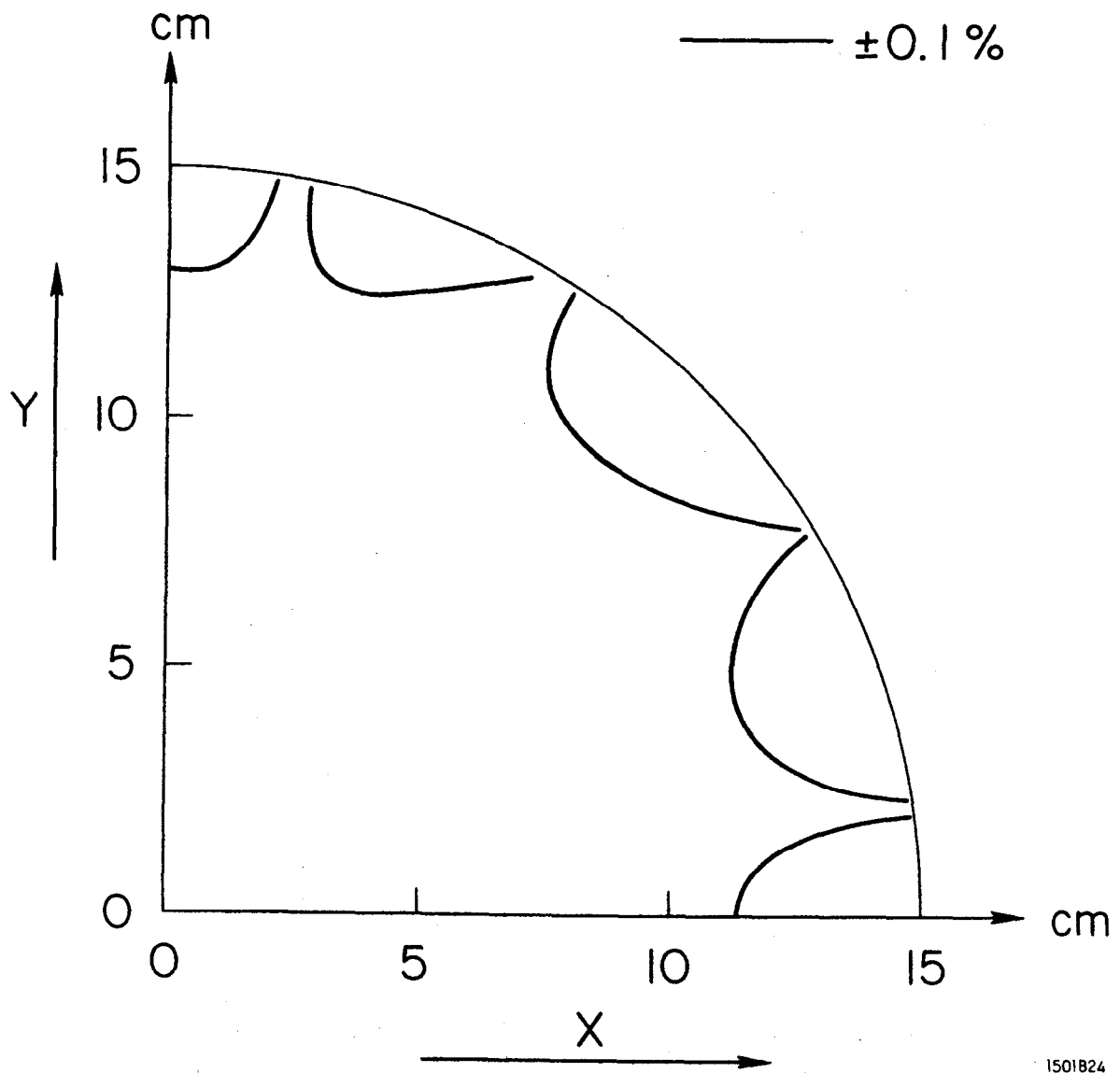


Fig. 23

1501824

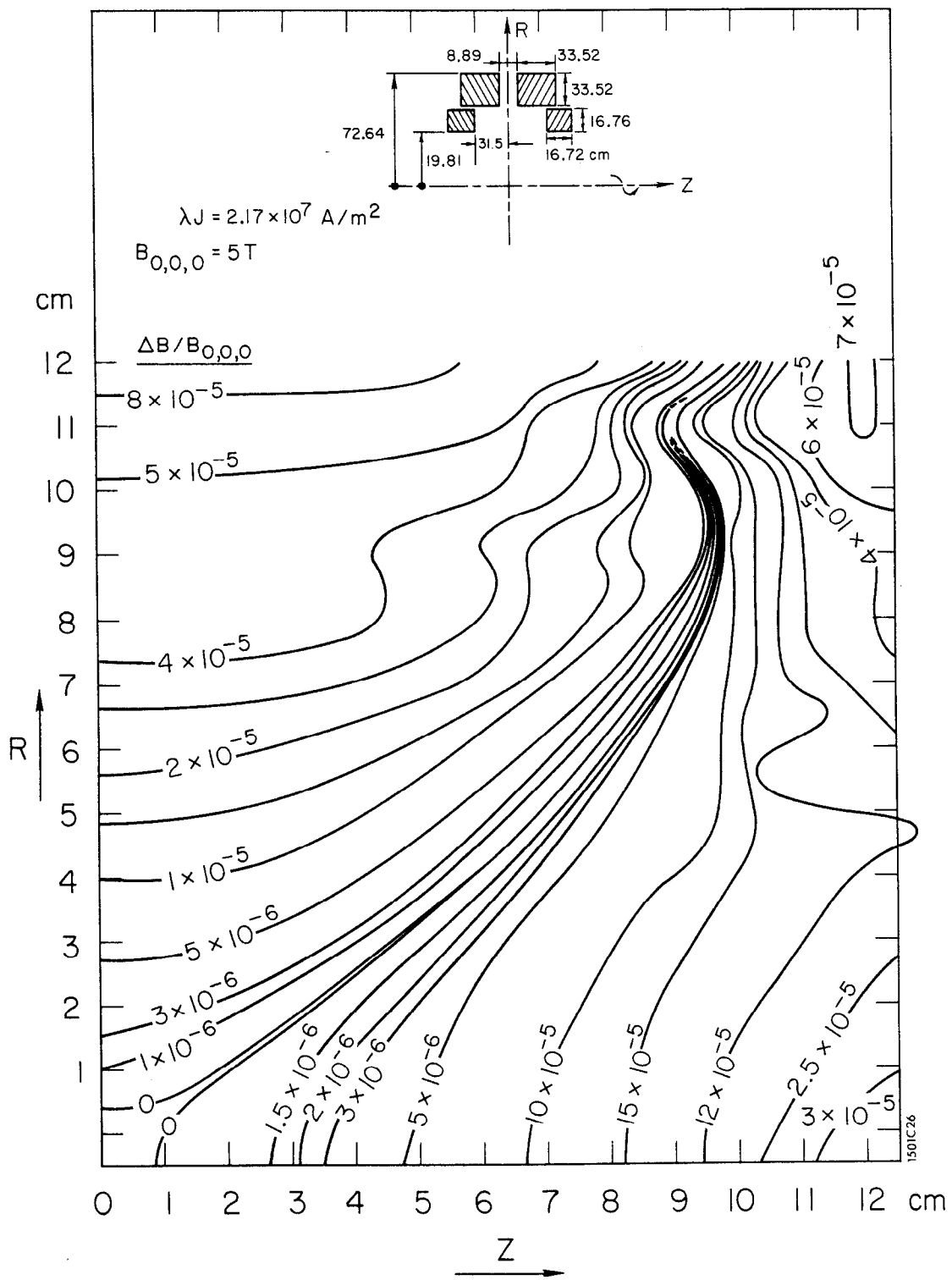


Fig. 24

